UNIVERSITÀ DEGLI STUDI DI PADOVA

DIPARTIMENTO DI FISICA E ASTRONOMIA GALILEO GALILEI

TESI DI LAUREA MAGISTRALE IN FISICA

Non-equilibrium fluctuations in GUVs driven by light

Laureanda:
Melissa RINALDIN

Relatore:
Prof. Dr. Antonio TROVATO
Correlatori:
Prof. Dr. Thomas SCHMIDT
MSc. Wim POMP
Controrelatore:
Prof. Dr. Mario BORTOLOZZI

Anno Accademico 2014-2015

Colophon

This report is based on the the work I have carried out in the last semester of my Master in Physics. The experiments were attained in the Cell Observatory at Leiden University with the *Fysica van Levens processen* (FvL) group, directed by Thomas Schmidt.

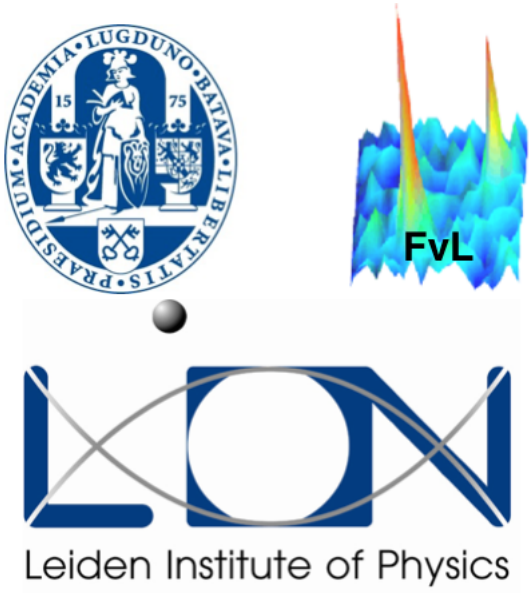

"Education is the point at which we decide whether we love the world enough to assume responsibility for it, and by the same token save it from that ruin which except for renewal, except for the coming of the new and the young, would be inevitable. And education, too, is where we decide whether we love our children enough not to expel them from our world and leave them to their own devices, nor to strike from their hands their chance of undertaking something new, something unforeseen by us, but to prepare them in advance for the task of renewing a common world."
-*Hannah Arendt*

Wassily Kandinsky, 'Circles in a Circle' (1923)

From more than one century ago to nowadays one of the main challenges in neurobiology is the understanding the basis of memory. The *locus* that was discovered to be the storage of memories in the mammalian brain, where the synapses are built on, are the dendritic spines.

The relation between molecular, morphological data of dendritic spines and memory formation with relative diseases has been extensively investigated, nevertheless many mechanisms are still poorly understood. One of these is *the compartmentalisation*, a term that involves the confinement of membrane-bound receptors in the head of spines and it is believed to underlie the changes in synaptic strength during learning and memory formation. One process proposed to explain the compartmentalisation is the presence of domains that trap the receptors from the surrounding.

In this work a biomimetical model was built to study the problem of the receptors confinement in dendritic spines.

By micromanipulation it is possible to model the spines with a well-controllable system in vitro made of one-layer lipid membranes with a spherical shape, named Giant Unilamellar Vesicles, (GUVs) and tubules. From previous studies it is known that when GUVs are prepared with lipids of different transition temperatures, at a critical composition, as the temperature is lowered, phase separation in Liquid Ordered (L_o) and Liquid Disordered (L_d) phases occurs.

In this work, a novel cutting-edge technique to obtain the phase separation is employed in a systematic way and the response of the GUVs is characterised in term of physical parameters. Briefly, the temperature is kept constant, and the composition of the vesicles changed using light, via *photo-oxidation*. Varying the ratio between the lipids that prefer the L_o and L_d phases until the critical composition is reached, it is possible to control the process and induce the phase separation for one vesicle of a time. In this way, the phase separated domains of the GUVs are used to model the compartments in the spines and quantum dots were added to the previous system mimic the receptors.

It is worthy to highlight the importance of using a biomimetic model to study this problem. It is a way to look in the heart of the process with different eyes, aimed not to neglect the detail of the system, but to provide a solid basis that allows to include all of them later and study the real problem with its complexity.

Contents

Introduction

The human brain consists of a hundred billion neurons interconnected into functional neuronal circuits that underlie all our behaviours, thoughts, emotions, dreams and memory [1]. The connection between neurons are called synapses: the continuous flow of signals through them is the basis of our lives. Most synapses of the human brain are formed by tiny dendritic protusions, named *dendritic spines*. Experimental evidence has shown that changes in spine morphology account for functional differences at the synaptic level [1–4]. Therefore the study of the morphology related to the function is of critical importance to understand the molecular mechanisms that underlie learning and memory.

One way to do this is to make an artificial model that mimics the dendritic spine using Giant Unilamellar Vesicles (GUVs) and tubules to model the head and the neck of the spines respectively [5]. GUVs are closed, spherical lipid bilayers of 10-100 μm diameter that can be produced from a broad range of lipid compositions in physiologically relevant buffer conditions. The more common and stable method to create them is via electroformation, a technique described for the first time in 1986 by Angelova et al. [6].

Lipid bilayers undergo complex physical behaviour. At high temperatures, all lipids in the bilayer mix uniformly in a single liquid phase. As the temperature is lowered, a transition occurs and the lipids separate into coexisting liquid phases: the liquid ordered (L_o) and the liquid disordered (L_d) phases [13, 14]. Lipids in each phase are distinguished by the degree of order in the acyl chains, which is higher in the L_o phase than in the L_d phase. Fluorescently labeled lipids partition differently into L_o and L_d phases of membranes, which allows imaging of different phases. Temperature and composition dependence of lipid mixing/demixing transitions have been investigated extensively [14, 16–19]. The composition and phase partitioning dependence of lipid diffusion as well as fluid domain diffusion has been analysed [15]. Three-dimensional membrane shapes modulated by differing elastic properties of coexisting liquid phases have been described [13, 14, 20]. Quantitative analysis of these shapes has confirmed aspects of elastic membrane theories [13, 21].

Although these phenomena present interesting soft condensed matter physics problems, research in this area is especially driven by the vivid discussion surrounding functionally important lipid/protein membrane heterogenities in living cells [24].

In the recent years, the observation of the effects of photo-oxidation in biological samples during imaging [25, 26], suggested to start to analyse the oxidative stress on membranes in detail [27–30]. In particular, the process of lipid oxidation has been associated with tubule formation, membrane budding, increases in membrane surface area, decreases in membrane fluidity and promotion of phase separation [58]. In this work, we used the photo-oxidation of lipids in a systematic way to induce phase separation in GUVs.

There are many benefits of this technique respect the one that uses the temperature. Firstly, it is possible to obtain the phase separation for one GUV of a time instead of all the sample at the same time, secondly it allows to control the process changing the intensity of the light and observe it at accessible times.
On 20 December 2013, the UN General Assembly proclaimed 2015 as the International Year of Light and Light-based Technologies. The potential of light and its applications are renewed in various fields. Among others, we recall the controlled use of oxidative stress, the mechanism studied in this thesis, that is useful in treatment of some diseases in photodynamic therapy (PTD).
Using light it is possible to induce structural changes in a system in a controlled

way, this is way we used it in our experiment.
In the first chapter we will introduce the neurobiological framework of the problem with an in-depth analysis of what happens at dendritic spine level. In chapter 2 we will describe the materials and methods employed in the system. In particular we will focus on membranes and single molecule fluorescence microscopy. In the third chapter we will report the state of the art experiments and in chapters 4 - 5 we will present the results.

Chapter 1

The Neurobiology of learning and memory

1.1 The locus of memory

1.1.1 Synaptic Plasticity

What changes are happening in your brain while you are reading this thesis? What is the *place* where the information that you are reading is stored? And how is learning made possible? *Your brain is not making new space to store the new memories, otherwise you head would become bigger and bigger!*
What happens is that the connections between neurons strengthen. This process is called *Long Term Potentiation* (LTP) and it is the ability of the synapses to change their strength as a result of their own activity or through activity in another pathway. It is a great example of *synaptic plasticity*, a term that involves several processes by which the brain undergoes neural changes.
Neurons communicate using electric-chemical signals through a junction between them called synapse. It is made of a pre-synaptic neuron, that is the neuron meeting up the synapse and a post synaptic neuron which is the neuron immediately following the synapse.
When the pre-synaptic neuron is stimulated it releases neurotransmitters which bind to the receptors of the post-synaptic neuron opening channels that allow ions like sodium and calcium to flow inside.
All neurons have a surrounding membrane and the interior has a different electrical charge than the exterior of the membrane and this difference in charge is called *action potential*. The number of the ions that flow in the post-synaptic neuron affect that difference. This is how we measure the strength of the synapse, by how much the post-synaptic neuron's potential changes as a result of pre-synaptic stimulation. With repeated stimulation, the same level of pre-synaptic stimulation converts into post-synaptic potential.
After the pre-synaptic neuron gets a lot of practice sending signals to a post-synaptic neuron, it gets better at sending those signals, and will get better at opening the channels to allow more ions inside. When this happens, we say that the synapse strength is increasing. When this increased strength lasts for a time, meaning anywhere from a few minutes to many months, it is called LTP [32].
This is thought to be the physiological mechanism by which learning occurs.

As synapses are strengthened and retain their strength, we are able to more easily recall previous experiences (figure 1.1) [32].

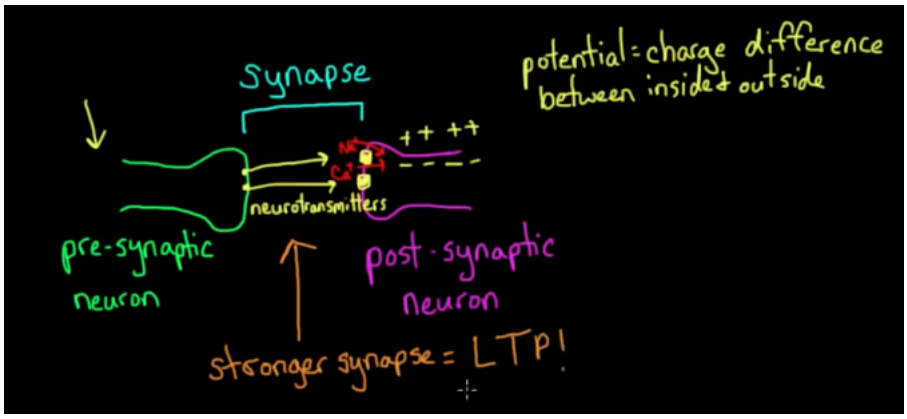

Figure 1.1: Long term potentiation and synaptic plasticity [32].

1.1.2 An insight into the dendritic spines

More than one century ago, soon after Ramón y Cajal first described the dendritic spine, it was proposed that the spine is likely to be the locus of long-term synaptic plasticity that it is associated with the storage of memories in the brain [1–4]. Since its conception, this dogma has been supported by indirect, correlative and anedoctal observation; for instance enriched environment enhances spine formation, and mentally retarded children express immature spines 1.3.
Briefly, dendritic spines are morphological specialisations that protube from the main shaft of neuronal dendrites (figure 1.2, 1.3 A).Typically 0.5-2 μm of length, dendritic spines are found at a linear density of 1-10 spines per μm of dendritic length in mature neurons.
Electron microscopy studies have identified roughly three categories of spines based on their morphology; thin, filopodia-like protusions (“thin spines"), short spines without a well-defined spine neck (“stubby spines”) and spines with a large bulbous head (“mushroom spines”).
The last ones consist of three distinct compartments that are represented in figure 1.3. They have, from below:

- a delta-shaped base at the junction with the dendritic shaft
- a constricted neck in the middle
- a bulbous head contacting the axon

Most excitatory synapses in mature mammalian brain occur on spines, and a typical mature spine has a single synapse located at its head. Therefore dendritic spines represent the main unitary postsynaptic compartment for excitatory input.

Spines exist only on certain types of neuron and moreover are abundant in higher brain regions. It has become evident that many psychiatric and neurological disorders ranging from metal retardation to Alzheimer’s disease and addiction are accompanied by alterations in spines shape and density. Further evidence suggests

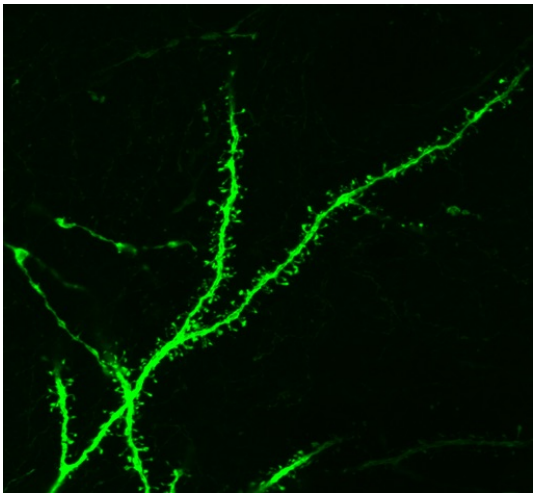

Figure 1.2: Confocal image of dendritic spines. (Jakub Jedynak)

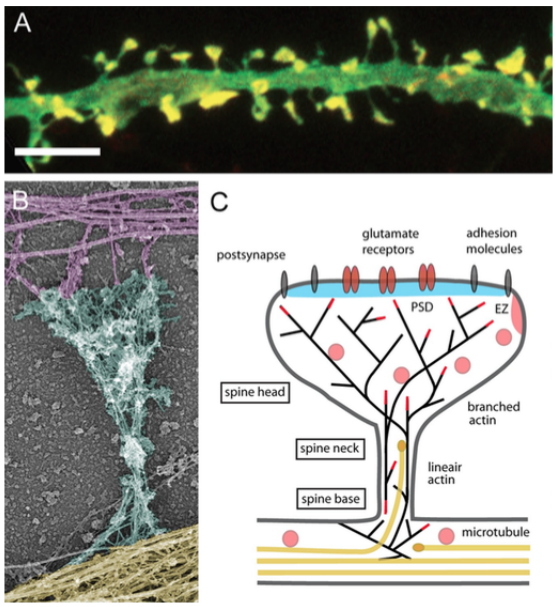

Figure 1.3: **Cytoskeletal organization of dendritic spines.** **A** Dendritic spine morphology (green) and localization of F-actin (red) in cultured hippocampal neurons. Bar 5μm. **B** Actin and microtubule cytoskeleton organization in a mature dendritic spine from cultured hippocampal neurons visualized by platinum replica electron microscopy (EM). Axonal cytoskeleton, purple; dendritic shaft, yellow; dendritic spine, cyan. The spine head typically contains a dense network of short crosslinked branched actin filaments, whereas the spine neck contains loosely arranged longitudinal actin filaments, both branched and linear. The base of the spine also contains branched filaments, which frequently reside directly on the microtubule network in the dendritic shaft. **C** Schematic diagram of a mature mushroom-shaped spine showing the postsynaptic membrane containing the postsynaptic density (PSD; blue), adhesion molecules (gray) and glutamate receptors (reddish brown), the actin (black lines) and microtubule (yellow) cytoskeleton, and organelles [1].

Factor/stimulus	Associated change in spine density
Visual deprivation	Reduction in spine numbers and spines with abnormal morphology along apical shafts of pyramidal cells in the rabbit visual cortex
Visual stimulation	Increased spine density in the rat visual cortex
Rearing in complex/enriched environment	Increased spine density in the CA1 region of the hippocampus or dorsolateral striatum of the rat
Hibernation	40% loss of spines in the squirrel hippocampus 91 during hibernation; spine numbers are recovered within hours of arousal
Sex steroid hormones	Female rats have more spines than males in a subset of hypothalamic nuclei and in the CA1 region of the hippocampus; spine density changes with the oestrus cycle in females
Stress	Spine density is enhanced in the hippocampus of 93 male rats, but reduced in the female hippocampus in response to an acute stressful event
Fragile-X syndrome	Spines are abnormally long and thin, and of increased density in the cerebral cortex
Down's syndrome	Spine density is markedly decreased in the hippocampus and cortex
Epilepsy	Spine density is decreased on hippocampal and neocortical pyramidal cells

Table 1.1: Environmental and disease factors that affect spine density [2].

that various memory disorders involve defects in regulation of actin cytoskeleton, the intercellular matrix that helps a cell with shape, support and movement.
Changes in spine density have also been observed in vivo, correlating with environmental factors that affect brain activity (Table 1.1).

1.1.3 The spines as dynamic structures

Live imaging studies have revealed that spines are remarkably dynamic, changing size and shape over timescales of seconds to minutes and hours to days.
Through the observation of spine dynamics over days it was seen and quantified that spine volumes grow and shrink spontaneously. Changing their shape, they exhibit some intrinsic fluctuations that contribuite to the structural dynamics of spines. These fluctuations reflect an inevitable lack of structural stability in spines.
At first glance, intrinsic fluctuations would seem incompatible with long term memory storage. However, two additional findings reveal that this variability does not defeat the maintenance of spine function over the time. Firstly, the volume of an

average spine remains largely the same for a certain period of time. Secondly, spine lifetimes can be very long, more than one year in vivo [4].
Spine dynamics concerned with long-term memory and cognition; intrinsic fluctuations in volume and a rapid, activity-triggered plasticity are cellular phenomena with implications for cognition and memory. Furthermore, impaired spine dynamics can cause psychiatric and neuro-developmental disorders. Schizophrenia and mental retardation and autism can arise from selective impairments in activity-dependent plasticity and intrinsic fluctuations, respectively.
Intrinsic fluctuations also predict the spontaneous generation of abundant new spines, leading to the random generation and test model of memory acquisition.
The biophysical properties of these fluctuations could mirror the psychological properties of complex behaviours, such as memories [2, 4].

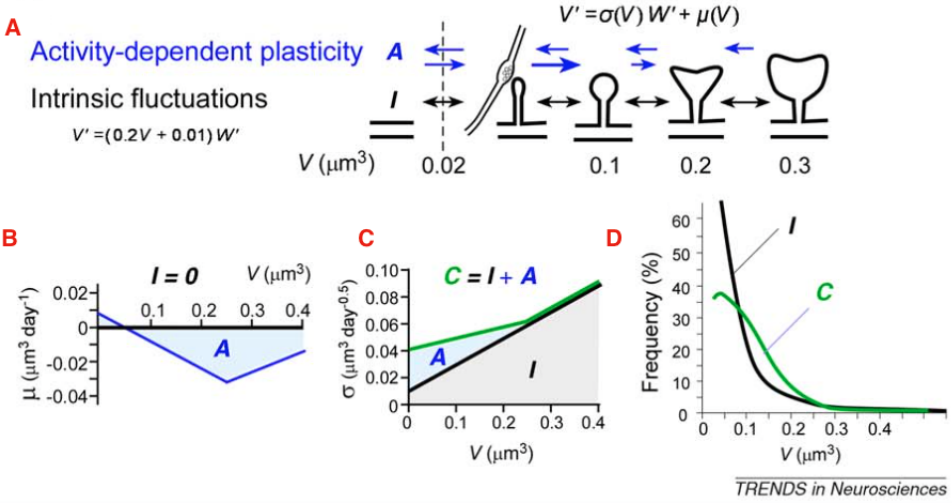

Figure 1.4: Long term structural dynamics of dendritic spines. **A** There are two mechanisms controlling the long term dynamics of spine volumes: activity dependent plasticity (A, blue arrows) and intrinsic fluctuations (I, black arrows) **B** Mean values of fluctuations in spine head volume in the presence (black) or absence (blue) of NMDA receptor inhibitors. **C** Standard deviation of fluctuations in spine head volume in the presence (black) or absence (green) of receptor inhibitors. **D** Probability-density distributions predicted from the C and I data given in B and C [4].

1.1.4 Dendritic spines form dynamic compartments

Since the discovery by Ramón y Cajal it has been suggested that spines play a role in the compartmentalisation of synaptic signals [8]. In spines there is compartmentalisation of:

- biochemical signals
- electrical signals
- membrane-bound receptors

Here we focus on the third type of confinement.
It is accepted that the lateral diffusion of receptors through the plasma membrane

regulates the mechanisms for synaptic plasticity. A large number of studies in vitro and in vivo, that are summarised in the work of Adrian et al. [8], were carried out to throw light on the mechanisms that regulate receptor confinement. Despite that, the regulation of receptors in spines is currently under debate. Experiments revealed slow diffusion coefficients of receptors in mushroom shape spines and reduced diffusion speeds in spine necks. Many processes were addressed to explain these results, here we recall the main interesting. First, the spine neck is believed to be a diffusion barrier for membrane bound proteins that regulate receptor diffusion in the spine compartment [9]. Second, the curvature of the spine head is proven to facilitate receptor trapping in the spine head [10]. And finally, we believe that in the mushroom head of spines L_o and/or L_d domains are present and act as confinement regions for the receptors.
Previous evidence of this mechanism was discovered studying the P2X3 receptor that was found localised in L_o domains of neuronal cells [11].

1.1.5 On modelling the dendritic spines

Despite the availability of a great quantity of data both in vitro and vivo to neurobiologists, the comprehension of the mechanical basis of learning and memory still has a lot of unclear aspects. One way to gain insight into them is to build biomimetic models to understand these processes in a consistent and controllable environment. In this regard, in this lab dendritic spines with a mushroom-like shape were mimicked with Giant Unilamellar Vesicles (GUVs) and tubules figure 1.5. Using GUVs instead of real spines allows to study the functionality of them in the easiest way, without the inconvenient presence of proteins.

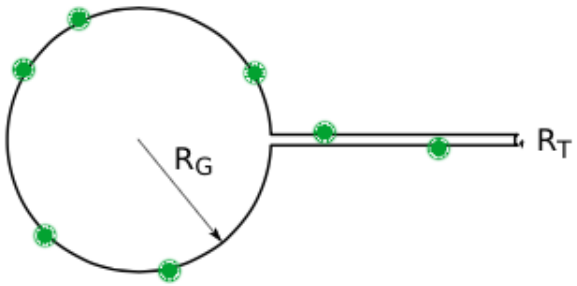

Figure 1.5: Biomimetic model of a dendritic spine made of a GUV and a tubule. R_G and R_T refer to the GUV's and tubule's radii respectively. [5]

In a previous study [5] the morphology dependence on receptor trapping has been analysed . To model the receptors, quantum dots were employed. They are represented with green dots in figure 1.5. Here we report the main results obtained. The motion of the quantum dots inside the GUVs was followed using single particle tracking. The traces of the quantum dots in the GUV and the tubule are represented in figure 1.6 A.
Data for different systems GUV+tubule displays a dependence of the diffusion coefficients on GUV size.
It was found for the rate E:

$$E = \frac{n_{esc}}{N} \cdot f$$

where: n_{esc} is the total number of escaped particles during the measurements, f is the framerate, N is the total number of particles in the GUV, at which the particles get away from the GUVs and go into the tubules scales as:

$$E \propto {R_G}^{\alpha} \qquad \alpha = 2.85 \pm 0.47$$

The dependence is shown in figure 1.6 B.
It is fascinating to see how addressing this subject to a modelling point of view reproduces the same results obtained in vivo with the real system.

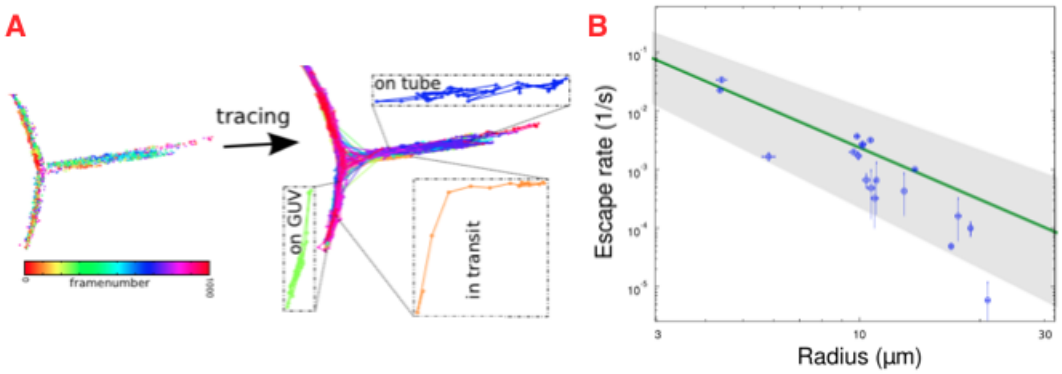

Figure 1.6: **A** Quantum dots traces **B** Dependence of the escape rate E on GUVs radius [5].

Chapter 2

Systems and techniques

2.1 The Physics of Vesicles

2.1.1 From lipids to bilayers

Lipid molecules constitute about 50% of the mass of most animal cell membranes, nearly all of the remainder being protein.
There are approximately $5 \cdot 10^6$ lipid molecules in a $1\mu m \cdot 1\mu m$ area of lipid bilayer.
All the lipid molecules in the plasma membrane are amphiphilic, that is, they have a hydrophylic, or *water loving*, end and a hydrophobic, or *water fearing*, end.
The most abundant membrane lipids are phospholipids. These have a polar head group and two hydrophobic hydrocarbon tails. One tail typically has one or more cis-double bonds (that is, it is unsaturated) while the other tail does not (that is, it is saturated). Each cis-double bond creates a kink in the tail.
The shape and the amphiphilic nature of the molecules cause them to form bilayers spontaneously in aqueous environment. They can do it in two ways: they can form spherical micelles, with the tails inward, or they can form double layered sheets, or bilayers, with the hydrophobic tails sandwiched between the hydrophilic head groups. Depending on the shape, these are called planar or spherical bilayers. The lipid vesicles are the spherical bilayers (figure 2.1).

The lipid bilayer is a continuous double layer about 5 nm thick where lipid molecules are arranged facing each other. It provides the basic fluid structure for all cell membranes and is easily seen by electron microscopy (fig. 2.1.1).
The fluidity of the lipid bilayer is crucial to many membrane functions and has to be precisely regulated. Certain membrane transport processes and enzyme activities, for example, cease when the bilayer viscosity is experimentally increased beyond a threshold level [33].

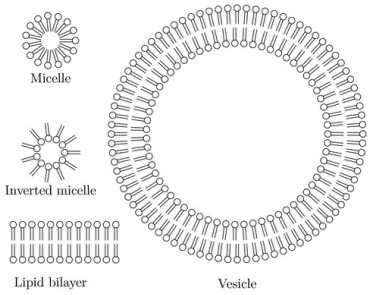

Figure 2.1: Schematic representation of a micelle, a planar bilayer and a vesicle.

The fluidity of a lipid bilayer depends on both its composition and its temperature as is largely demonstrated in studies of synthetic bilayers [12–14].
A synthetic bilayer made of a single type of phospholipid changes from a liquid (liquid disordered) state to

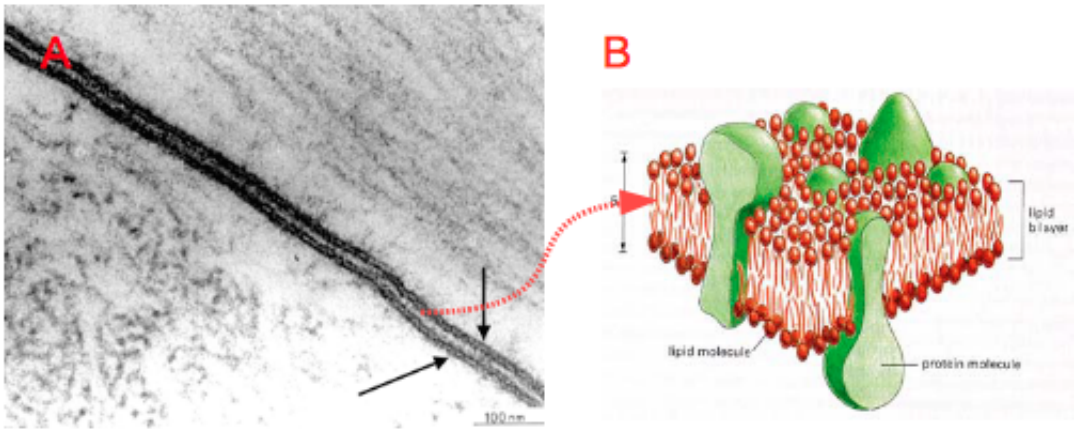

Figure 2.2: **A** Plasma membranes of two cells (indicated by the two arrows), with an intercellular space between them. **B** Three-dimensional view of a cell membrane

a liquid crystalline ordered state at a characteristic point. This change is called *phase transition* and the temperature at which it occurs is lower if the hydrocarbon chains are short or have double bonds.
A shorter chain length enhances the tendency of the hydrocarbon tails to interact with one another, in the same and opposite monolayer, and the *cis*-double bonds produce kinks in the hydrocarbon chains that make them more difficult to pack together, so that the membrane remains fluid at lower temperatures.
Cholesterol modulates the properties of lipid bilayers. When mixed with phospholipids, it enhances the permeability-barrier properties of the lipid bilayer. It inserts into the bilayer with its hydroxyl group close to the polar head groups of the phospholipids, so its rigid, platelike steroid rings interact with and partly immobilise those regions of the hydrocarbon chains closest to the polar head groups.
Analysis of membrane lipids by mass spectrometry has revealed that the lipid composition of a typical cell membrane is much more complex than originally thought. According to these studies, membranes are composed of a variety of 500-1000 different lipid species [33].

2.1.2 Synthetic Vesicles

The influence of lipid composition on physical and chemical properties of the membrane can best be studied in a model system which allows complete control over the membrane's composition.
The liposomes made of artificial membrane allow to carry out systematic measurements of mechanical and rheological properties of bilayers as a function of membrane composition and temperature, as well as hydrodynamic interactions.
Vesicles are membranes with a spherical shape formed by bending and closing up a lipid bilayer (figure 2.1). Various experimental techniques have been developed for preparing liposomes of different sizes (from nanometers to tens of microns).
Large sizes can be obtained from vesicles made of only one bilayer. The largest (several tens of microns) vesicles are called giant unilamellar vesicles (GUVs), vesi-

cles with one lipid bilyer, and are an extraordinarily convenient system for studying membrane behaviour. They are well visible under an optical microscope and thus allow for direct manipulation and observation of membrane interactions. In contrast, working with conventional vesicles (a few hundreds of nanometers) usually involves the application of indirect methods and techniques for observation. Their small size often raise questions about effects due to membrane curvature when molecular interactions are considered. In contrast, giant vesicles that have a size in the micrometer range, i.e. are of cell-size, reflect the membrane properties and behaviour in cells.
There are many techniques for vesicle formation. For example one is based on the effect of electric fields, or electroswelling, and another one is called spontaneous swelling (or gentle hydration) [54]. In this thesis we employed the first one.
The electroswelling technique provides a high yield of unilamellar vesicles of controllable lipid composition and size. Briefly, lipids are dissolved in an organic solvent and dried on the plates of a capacitor. The space between the plates is filled with an aqueous buffer and an oscillating electric field is applied. On the time scale of hours the electric field causes vesicles to swell from the lipid film and continue to grow by fusion.
With electroformation it is possible to produce vesicles that consist of a mixture of phospholipids, cholesterol and sphingolipids, mimicking the composition of a cell membrane [12].

2.2 Fluorescence Microscopy

2.2.1 Introduction

The technique of fluorescence microscopy has become an essential tool in biology and the biomedical sciences, as well as in materials science due to attributes that are not readily available in other contrast modes with traditional optical microscopy.
The large spectral range of available fluorophores allows simultaneous imaging of different cellular, subcellular or molecular components. The rapidly advancing innovations of laser scanning confocal and two photon microscopes mean that fluorescence approaches now provide a powerful approach to seeing deep tissues. Recent techniques like light-sheet fluorescence microscopy allow to obtain 3D imaging at high spatiotemporal resolution [36]
From its name, the process that underlies the fluorescence microscopy is *the fluorescence*. Fluorescence is the emission of light that occurs within nanoseconds after the absorption of light.
The basic function of a fluorescence microscope is to irradiate the specimen with a desired and specific band of wavelengths, and then to separate with a filter the much weaker emitted fluorescence from the excitation light. In a properly configured microscope, only the emission light should reach the eye or detector so that the resulting fluorescent structures are superimposed with high contrast against a very dark (or black) background. The limits of detection are generally governed by the darkness of the background, and the excitation light is typically several hundred thousand to a million times brighter than the emitted fluorescence. The background light usually consists of out-of-focus light.

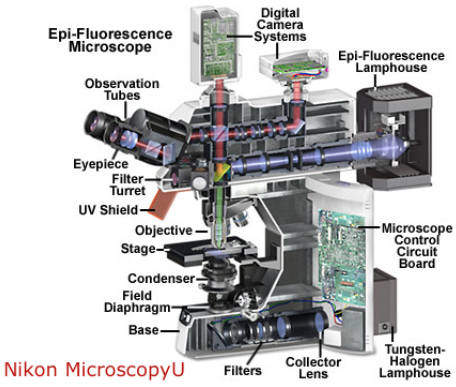

Figure 2.3: Diagram of a modern fluorescence microscope equipped for both transmitted and reflected fluorescence microscopy. The basic function of a fluorescence microscope is to irradiate the specimen with a desired and specific band of wavelengths, and then to separate the much weaker emitted fluorescence from the excitation light [34].

An useful tool to understand the processes of the excitation and emission is the Jablonski diagram, conceived by Alexander Jablonski in the 1930s. This diagram displays the energy states of a fluorophore [1] (figure 2.4)

[1] The fluorescent molecules are named fluorophore or dye.

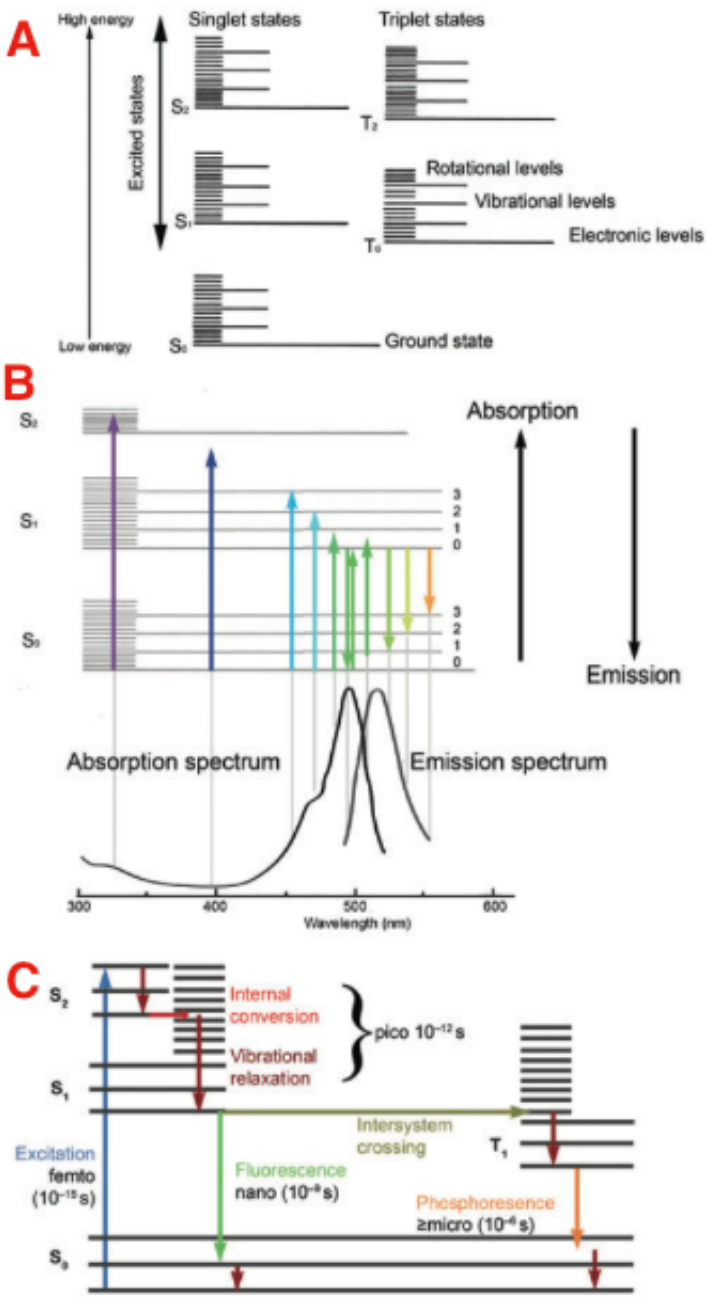

Figure 2.4: **A** Jablonski diagram displaying the energy states of a molecule. **B** Absorption and emission spectra of a common fluorophore with the Jablonski diagram. The vertical grey lines aligns the spectra with the energy of absorbed or emitted photons. The coloured arrows represent the wavelenghts of the photons. **C** The times that the various steps in fluorescence excitation and emission and phosphorescence take [35].

2.2.2 Absorption, excitation, emission

In a typical fluorophore, irradiation with a wide spectrum of wavelengths will generate an entire range of allowed transitions that populate the various vibrational energy levels of the excited states. Some of these transitions will have a much higher probability than others, and when combined, will constitute the absorption spectrum of the molecule.
When a fluorophore absorbs the excitation light, all the energy possessed by a photon, expressed by Planck's law

$$E = h\nu \qquad \nu = \frac{c}{\lambda}$$

is transferred to the fluorophore. The absorption of a photon of energy by a fluorophore, which occurs due to an interaction of the oscillating electric field vector of the light wave with charges (electrons) in the molecule, is an all or none phenomenon and can only occur with incident light of specific wavelengths known as absorption bands.
With ultraviolet or visible light, common fluorophores are usually excited to higher vibrational levels of the first (S_1) or second (S_2) singlet energy state. Immediately following absorption of a photon, several processes will occur with varying probabilities, but the most likely will be relaxation to the lowest vibrational energy level of the first excited state (S_1). This process is known as internal conversion or vibrational relaxation (loss of energy in the absence of light emission) and generally occurs within picosecond or less. An excited molecule exists in the lowest excited singlet state (S_1) for periods on the order of nanoseconds (the longest time period in the fluorescence process by several orders of magnitude) before finally relaxing to the ground state (S_0). If relaxation from this long-lived state is accompanied by emission of a photon, the process is formally known as *fluorescence*. The closely spaced vibrational energy levels, when coupled with normal thermal motion, produce a wide range of photon energies during emission. As a result, fluorescence is normally observed as emission intensity over a band of wavelengths rather than a sharp line.
Several other relaxation pathways that have varying degrees of probability compete with the fluorescence emission process.
The excited state energy can be dissipated non-radiatively as heat or the excited fluorophore can collide with another molecule to transfer energy in a second type of non-radiative process. The latter event is relatively rare, but ultimately results either in emission of a photon or a transition back to the excited singlet state that yields delayed fluorescence.
Transitions from the triplet excited state to the singlet ground state are forbidden, which results in rate constants for triplet emission that are several orders of magnitude lower than those for fluorescence.

2.2.3 The fluorescence microscope

In a fluorescence microscope (figure 2.3) first the specimen is illuminated with one wavelength and the returned light is filtered only to see longer wavelength-shifted fluorescence. A common light source is the arc lamp in Kohler-style illumination.

In the modern fluorescence microscopy the preferred configuration is epi-illumination. This setup uses the objective both to illuminate and image the specimen. The advantage of this approach over transmission fluorescence microscopes (in which the exciting light comes through the condenser and the emission is collected by the objective) is that only the small percentage of the exciting light that is reflected off the sample needs to be blocked in the return light path in the epi-illumination mode. This approach requires a special kind of beam splitter, called dichroic mirror to separate the excitation from the emission. The dichroic reflects shorter wavelength light originating from the light source and transmits the longer wavelengths of the emitted fluorescence. Each dichroic is designed to have a transition from reflection to transmission that resides between the excitation and emission peaks of the fluorophore it is designed to be used with (fig. 2.5 b). The dichroic is used with two additional filters: the excitation filter, that preselects the excitation wavelength[2], and an emission filter that only allows passage of the longer wavelength light back to the detector.

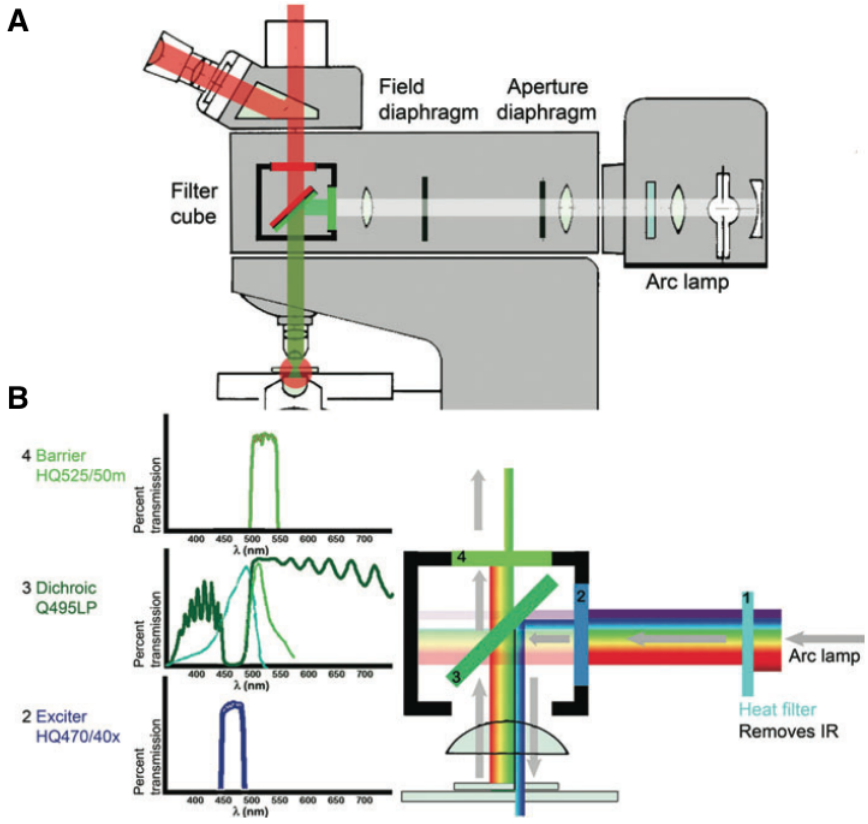

Figure 2.5: The fluorescence microscope **A** Epi-illumination fluorescence microscope. **B** Dichroic mirror to excite and detect the fluorophore GFP. The main three components (2,3,4) have specific spectral features that are ideal for GFP [35].

Because the microscope objective is both the source of light that excites the fluorescence in the specimen and the optical element that collect the fluorescence, its

[2]Our setup does not have excitation filters because we use lasers with well-defined wavelengths.

properties have a large impact on the fluorescence image. The more important parameter to characterise the objective is the *numerical aperture* NA, that is equal to:

$$NA = n \sin(\alpha)$$

where n is the index of refraction of the medium between the objective and the coverslip and α is the angle between the vertical and most extremely angled ray that can be collected by the objective.
The numerical aperture sets both the resolving power that is

$$d = \frac{0.61\lambda}{NA}$$

and the light efficiency for the objective. About the last one, since the larger α is, the greater number of photons can be collected and the greater the amount of light that can be used to excite the specimen, the amount of exciting light through an objective is roughly proportional to $(NA)^2$. In the same way, also the amount of the fluorescence emission collected is also proportional to $(NA)^2$, therefore the intensity observed is proportional to $(NA)^4$.

2.2.4 The phenomenon of bleaching

Although in principle a fluorophore can cycle between ground and excited states an unlimited number of times, the conditions in which organic fluorophores are used usually limit the number of cycles. Estimates of 10000-40000 cycles are often cited as the limit before permanent bleaching occurs for good fluorophores [35]. Bleaching is a generic term for all the processes that cause the fluorescent signal to fade permanently.
At molecular level there are several different ways bleaching can occur. It is clear that the long-lived triplet state provides more opportunities for a molecule with an excited electron to interact with other molecules than the briefer singlet states. Hence, more bleaching is thought to be associated with triplet states. It also appears that one of the important ingredients in bleaching is an interaction between a triplet state fluorophore and molecular oxygen. The triplet state can transfer its energy to the oxygen, exciting oxygen to its singlet excited state. Singlet oxygen is a reactive molecule that can participate in many kinds of chemical reactions with organic molecules. These chemical reactions can covalently alter the fluorophore to inactivate its ability to fluoresce. In addition, the singlet oxygen can interact with other organic molecules causing phototoxicity for living cells [3] [34, 35].

[3] This is the mechanism of photo-oxidation that will be described later and used in this thesis.

2.3 The single molecule level

2.3.1 Introduction to single molecule experiments

There's plenty of room at the bottom.
- Richard Feynman, Caltech December 1959 [37]

In his talk named *Plenty room at the bottom* the nobelist Richard Feynman inspired several generation of scientists to seek to fill *this room* with nanometer scale materials and techniques to study them. From the 1980s numerous and powerful techniques to both observe and manipulate single molecules were developed and refined. These techniques range from super resolution fluorescence microscopy, atomic force microscopy to optical and magnetic tweezers.
To date, single molecule microscopy has evolved into the ultimate-sensivity toolkit to study systems from small molecules to living cells, with the prospect of revolutionizing the modern biosciences [38]. In this work we have employed this technique to study the motion of single molecules at nanometer scale.
The base hypothesis to single molecule studies lies in the *ergodicity theory* [39] from statistical mechanics. According to this, a sufficient long time average (or sufficient number of observations) from a single molecule is equivalent to a standard population-averaged snapshot, suggesting that a single molecule experiment contains all the information of molecular ensemble.
Single molecule approaches:

- reveal heterogenity and disorder in a sample, albeit in a finite observation window
- afford precise localisation and counting of molecules in spatially distribuited samples such as living cell
- work at the low numbers observed for most specific biopolymers in a living cell eliminating the need for artificial enrichment
- enable the quantitative measurements of the kinetics or statistics of complex biological processes without the need for a perturbing synchronization of molecules
- reveal rare and/or transient species along a reaction pathway, which are typically averaged out in ensemble measurements
- facilitate the direct quantitative measurements of mechanical properties of single biopolymers and their assemblies, including the forces generated by biological motors
- provide a way *just look at the thing* as Feynman suggested, as one can argue that seeing single-molecule behaviour is believing

In figure 2.6 a flowchart of the main single molecule techniques available to answer biological questions is presented.

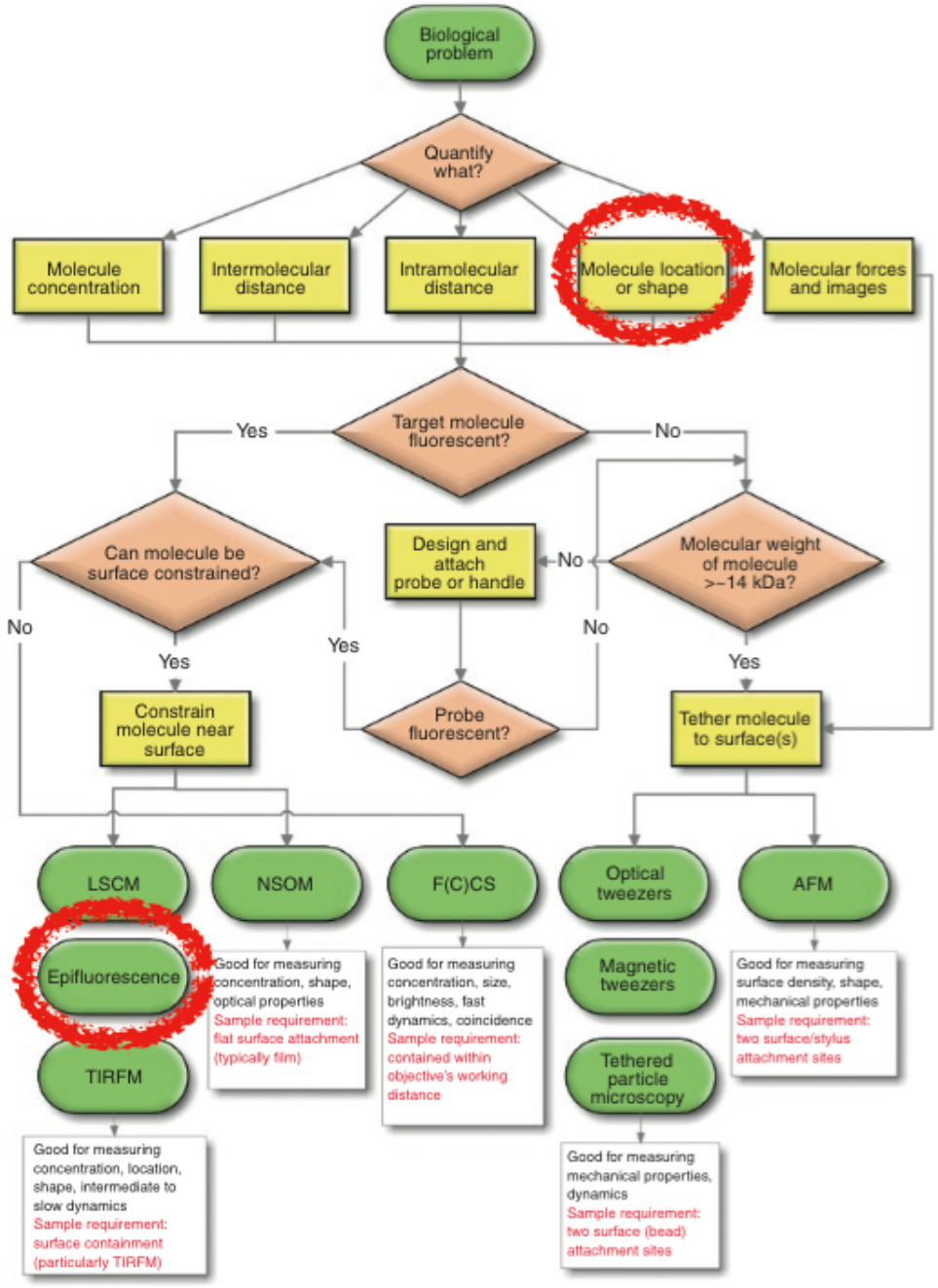

Figure 2.6: Flowchart to select a suitable single-molecule techniques to study a given biological problem. In red are circled the problem and the technique that this thesis deals with [42].

2.3.2 Single-molecule fluorescence microscopy

Single-molecule localisation

Over 120 years ago Ernst Abbe postulated that optical resolution is impossible below $\sim 200\ nm$. Many efforts to overcome this limit were attempted from that, and in particular one goal in biology was the observation of molecules in motion at high spatial and temporal resolutions. As early as 1996 it became possible, tracking of diffusive motions of membrane constrained, dye label single molecules was reported by Thomas Schmidt et al. with a spatial resolution of 14 nm [40] . Current ultrahigh-resolution fluorescence microscopy tools have advanced resolution of up to 1.5 nm [42,43]. The *heart* of the single molecule fluorescence microscopy is to localise and track single emitters (fluorophore molecules, quantum dots, beads) by finding the center of their diffraction limited point-spread functions (PSFs) in a sequence of wide-field images.
The PSF is given by the Airy disk, that has a width of:

$$w = \frac{0.61\lambda}{NA}$$

where λ is the wavelength and NA the numerical aperture. The center is found by approximating the PSF with a two-dimensional Gaussian function as we will describe. If we consider that the image is an arbitrary sum of point light sources $\vec{s}_i$, it can be described with the Gaussian function:

$$I(\vec{s}) = \sum_i N_i \frac{1}{2\pi w^2} e^{\frac{-(\vec{s}-\vec{s}_i)^2}{2w^2}}$$

where N_i is the number of emitted photons and w the width of the Gaussian. The Gaussian PSF predicts that the localisation accuracy σ_i for an individual emitter is given by

$$\sigma_i = \frac{w}{\sqrt{N_i}}$$

Contributions for the background noise b and the pixelation (with pixel size a) must be added [44,45]:

$$\sigma_i = \sqrt{\frac{w_i^2}{N_i} + \frac{a^2}{12N_i} \cdot \frac{8\pi {W_i}^4 b^2}{a^2 {N_i}^2}}$$

The process of the peak localisation is represented in figure 2.7 [40] .

Single-molecule tracking

The single molecule positions obtained from PSF fitting are the starting point for single particle tracking. The next step is to correlate the position of the molecules present at a time t_i to the position of the molecules present at a time t_{i+1}. Since the molecules undergo to Brownian motion, the trajectory and the diffusion coefficient can be calculated from one of the greatest results of Albert Einstein: *On the theory of Brownian Movement* [46].

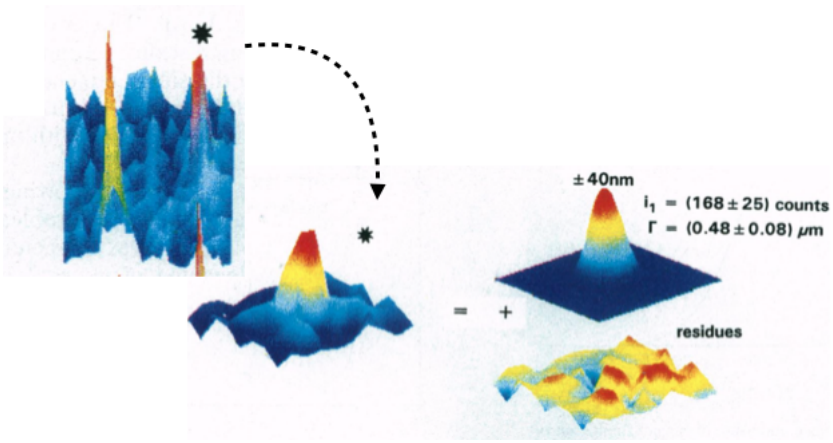

Figure 2.7: PSF modelled by a Gaussian. In the left the intensity distribution of a peak (marked with *) and on right the sum of the Gaussian fit and the residues are represented [40].

The motion of the molecules is calculated from the probability density function of the displacements $\vec{x}$ that is:

$$P(\vec{x},t) = \frac{1}{\sqrt{4\pi Dt}} e^{-\frac{\vec{x}^2}{4Dt}}$$

The square root of the displacement is given by

$$\sqrt{\vec{x}^2} = \sqrt{2dDt}$$

where D is the diffusion coefficient and d the dimension. This expression was found by Einstein as a solution of the Diffusion Equation [47]:

$$\frac{\partial n(x,t)}{\partial t} = -D\frac{\partial^2 n(x,t)}{\partial x^2}$$

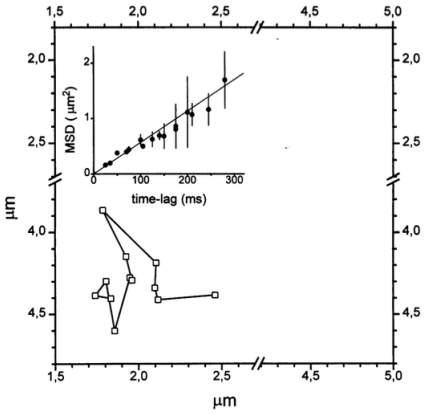

Figure 2.8: Diffusion of a single lipid molecule. In the inset the mean square displacement is plotted against the time-lag, which is the time between two frames [40].

for the initial condition $n(x,t_0) \propto \delta(x)$ In figure 2.8 we give an example of a trajectory of a single lipid molecule diffusing in a liquid.
Detailed information about the localisation and tracking method employed in this thesis will be given in Chaper 5.
Single molecule tracking allows to directly visualize the diffusion of single molecules. However, it suffers from fluorophore photobleaching which results in short trajectories [41]. This limitation can be overcome by using quantum dots or gold nanoparticles. In this thesis we used quantum qdots. Quantum dots are crystals of a fluorescent semiconductor material with a diameter of as few as 10 to 100 atoms (2-10 nm). They are used as labels for imaging molecules because of their very narrow fluorescence spectra, brightness and resistance to photobleaching.

Chapter 3

State of the art

3.1 Phase separated vesicles

3.1.1 Phase transitions

Phase transitions are common occurences in matter [48].
The term of phase separation indicates a transition from a single component system to a multicomponent system. The point at which the transition occurs is called critical point. According to Ginzburg when he was asked to give an *a list of especially important and interesting problems in physics a astrophysics* [49], the phase transitions represent some of the more challenging problems in solid state physics. It is thrilling for biophysicists to find that phase transitions occur in many and different biological problems. To introduce the phase transitions, we can consider the phase diagram of water in figure 3.1. As the temperature and pressure vary water can exist in solid, liquid, gas phases. Well defined phase boudaries separate the regions in which each state is stable while crossing the phase boundaries a jump in observables like density, latent heat occur.

Consider moving along the line of liquid+vapor coexistence. As the temperature increases the difference in density between the liquid and the vapor decreases continuously to zero. It becomes zero at the critical point beyond which it is possible to move continuously from liquid-like to a vapor-like fluid. The difference in densities, which become non zero below T_c, is called the order parameter of the liquid-gas transition [52]. Seen on this diagram the critical point looks no significant, however there are clues that this might not be the case. In second-order phase transition [1] the critical point is the point at which the response functions are discontinuous. This is the case for the surface tension measured for a liquid crystal that undergoes a phase transition (figure 3.2).

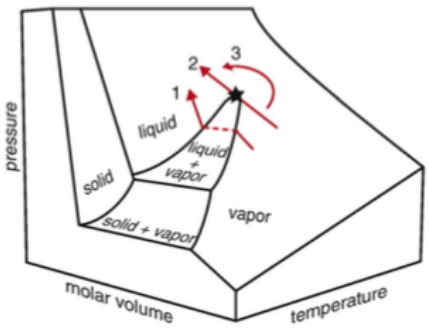

Figure 3.1: 3-dimensional phase diagram for water [50].

An interesting aspect of phase transition is the behaviour of the fluctuations.

[1] Ehrenfest classification

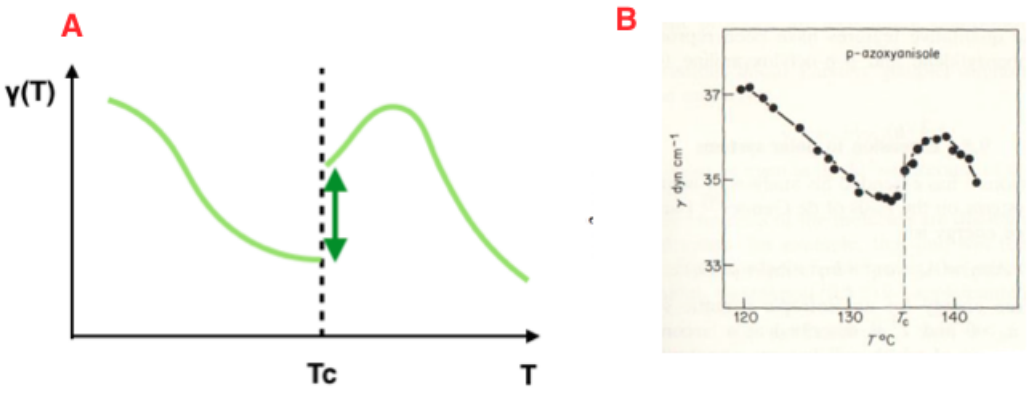

Figure 3.2: **A** Schematic of the variation of the nematic surface tension showing a discontinuity and subsequent inversion in the vicinity of the nematic isotropic transition temperature for a liquid crystal **B** Experimental data [53]

Near T_C, which is called the critical region, the interface energy between the two phases becomes as low as the thermal energy k_BT, which is Boltzmann's constant times the temperature. As a result, large, thermally-driven fluctuations occur. The fluctuations can be so large that we can see their effects by eye [50]. Even as far back as 1937, there was evidence of divergent fluctuations near the critical point, elegantly explained by Einstein, as evidenced by critical opalescence [2].
The salient behaviour of 2D systems at equilibrium very close to critical points is captured by the 2D Ising model, in which spins on a 2D lattice communicate only through nearest neighbour interactions.
The 2D Ising model produces a uniform, disordered phase at high temperature, two coexisting phases at low temperature, and fluctuations near the critical point.
One of the truly outstanding attributes of critical behaviour is that it is *universal*, meaning that many properties can be understood without considering the details of the system. This property is valid only if the process is an equilibrium process. If not, the universality is not valid anymore and the time-evolution depends on the detail of the system.

3.1.2 Phase separation in GUVs

Membranes formed from multiple lipid components with different melting temperatures can laterally separate into coexisting liquid crystalline phases, or domains, the liquid ordered (L_o) and the liquid disordered (L_d).
Both are charcterized by a high lateral mobility of the lipids, but they differ in the organization of the lipid tails. In the L_o phase, which is enriched in sphingolipids and cholesterol, the cholesterol intercalates between the sphingolipids and causes long range correlation between the lipid tails, hence this phase is called ordered. In the L_d phase which contains predominantly phospholipids, neighbouring lipid tails interact only weak, and, due to the kink in the unsaturated acyl chains, there are more possible tail configuration. Because of the lack of orientational correlation be-

[2] In the critical region due to the presence of large fluctuations the light scattering is so large that the substance appears milky white in reflected light and brownish dark in transmitted light.

tween the tails this phase is called disordered [12]. This process, which may resemble raft formation in cell membranes, has been directly observed in GUVs (fig. 3.3 [13]). At present, controversial opinions are proposed about the raft hypothesis, the ability of some liquid domains with high chain order to mediate protein interactions, and therefore cell signalling [55].

The method adopted until now to obtain phase separation is to prepare the GUVs with a critical composition at high temperatures (about 60^oC), and lower the temperature to reach the mixing/demixing temperature (that is about the room temperature) at which the phase separation happens. A critical composition is by definition a composition that can lead to phase separation, and it could be visualized with a point in the grey region of the phase diagram.
The phase diagram for a 3-component system is represented using a ternary plot (fig. 3.4 B).
A ternary plot is a triangular diagram which displays the proportion of three variables that sum to a constant and which does so using barycentric coordinates. The coordinate axes of such a diagram are shown in the figure 3.4 A, where each of the x,y, and z axes are scaled such that $0 \leq x, y, z \leq 1$, and where the grid lines denote the values $x, y, z = n/6,\ n = 1, 2, ..., 5$ for a ternary mixture of lipids.

Figure 3.3: ***Creative Tension: The forces that shape biological membranes.*** Cover of the issue of Nature of October 23, 2003 [13]

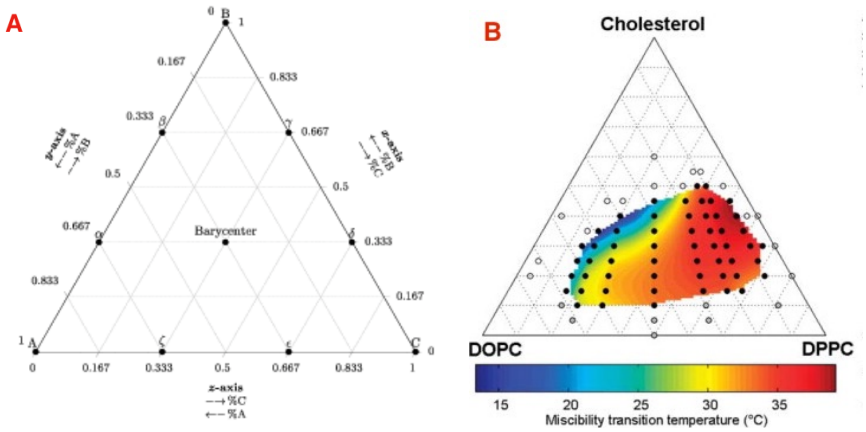

Figure 3.4: **A** Example of a ternary plot. **B** Ternary phase diagram of a mixture of (1,2-Dioleoyl-sn-glycero-3-phosphocholine) DOPC, (Sphingomyelin) SM and (Cholesterol) Chol. The region that is colored represent the composition that undergoes phase transition. The temperature at which the transition occurs is labelled with the colormap.

Detailed theoretical frameworks link the elasticity of domains and their boundary properties to the shape adopted by membranes and the formation of a particu-

lar domain patterns [13, 62]. Indeed, the geometry of phase-separated vesicles is theoretically obtained by minimizing the energy functional, which is named the Canham-Helfrich energy [56, 57].

$$\epsilon = \sum_{i=1,2} \int_{S_i} (2\kappa_i H^2 + \kappa_G^{(i)} G + \sigma_i) dA - pV + \tau \oint_{\delta S} dl$$

The subscript i refers to the two phases, $H = 1/R_1 + 1/R_2$ is the mean curvature and $G = 1/(R_1 R_2)$ is the Gaussian curvature. R_1 and R_2 are the principle radii of curvature.
The surface tension σ gives the energy needed to increase the membrane area with a unit area. The Laplace pressure p is the pressure difference between the inside and the outside and its value influences the shape of the vesicle. κ and κ_G are the bending and the Gaussian rigidity respectively. The bending rigidity represents the resistance under a bending deformation.The interfacial energy per unit length is called line tension τ. Since the total energy of the interface is proportional to the length of the interface, the energy of a vesicle is decreased by coalescence of domains. The ground state should therefore be a completely phase separated vesicle (figure 3.5) [12].

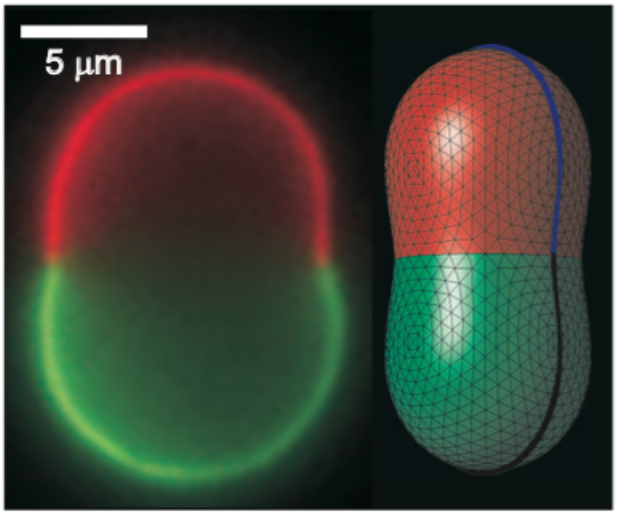

Figure 3.5: Left: image of a complete phase separated vesicle (equatorial section) in the peanut shape (Lo phase shown in red, Ld phase shown in green); Right: vesicle shape determined numerically by minimization of the Canham-Helfrich energy. [12]

3.1.3 Phase separation in GUVs as a critical process

In the last section we treated the phase separation of the GUVs saying that when they are prepared at a critical composition and pass through a critical temperature a transition occurs.
Since the temperature is of the order of room temperature, the GUVs are a a biophysical system that allows to study critical phenomena in the two-dimensional Ising university class.

The 2D Ising model produces a uniform disordered phase at high temperature, two coexisting phases at low temperature, and fluctuations near the critical point. The same behaviour occurs in membranes. Even though GUVs are a 3D object, since the thickness is very small (about 5 nm) they can be described as a 2D system˙ This evidence inspired Sarah Veatch [14, 16, 17, 19], that had long experience with membranes and phase separation, to carry out a quantitative study of the phase separation in GUVs in comparison to the 2D Ising universality class [50]. In her study, the fluctuations of the shapes of domains (figure 3.7) of GUVs at critical composition that exhibited phase separation at low temperatures were analysed, and from that the line tensions and the correlation length were determined.

The critical exponent from the line tension

$$\lambda = |T - T_c|^{-\nu}$$

and the correlation length

$$\xi \approx |T - T_c|^{\beta}$$

where T is the temperature and T_c is the critical temperature, were calculated and compared to those of the university class of the two dimensional Ising model.

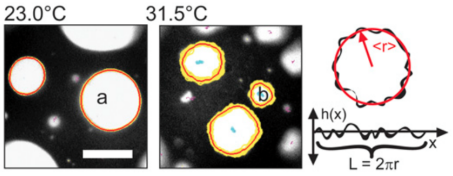

Figure 3.7: Images of domains of phase separated GUVs (left) and shape fluctuation of the boundary of the domains (right) [51].

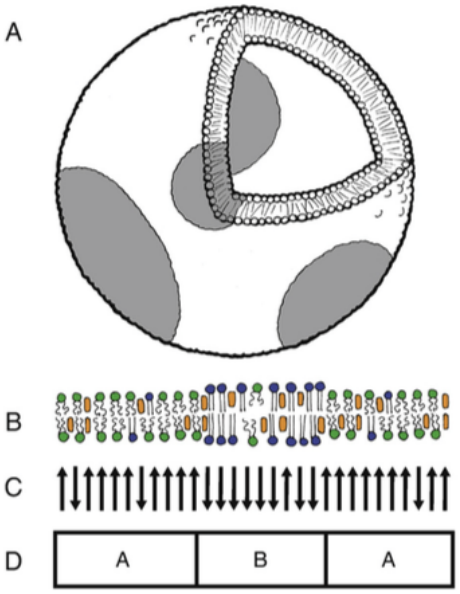

Figure 3.6: **A** A unilamellar vesicle is a thin spherical shell composed of a lipid bilayer, bound by water on the inside and outside. When the composition of the bilayer is a ternary mixture of a lipid with a high melting temperature, and cholesterol, the bilayer can contain micron scale coexisting liquid phases. **B** The two different phases contain different mole fractions of three lipid types. For a giant unilamellar vesicle of radius $> 20\ \mu m$, the lipid bilayer is essentially flat. The critical behaviour of this membrane is well described by **C** a 2D-lattice of *Ising spins* or **D** any equivalent thin sheet of material containing two states as long as the correlation length is greater than the thickness of the sheet [50].

3.2 Lipid Oxidation

Introduction

The oxidation of phospholipids has become a recent topic of interest within the field of membrane biophysics. The process of lipid oxidation has been associated with tubule formation and membrane budding, increases in membrane surface area, decreases of membrane fluidity and promotion of phase separation [26]. In synthetic bilayer systems, the presence of reactive oxygen species has been linked to both the formation of singlet oxygen $^1O_2$ from photo-induced oxidation and autoxidation. The first process is what we are interested in. The second process occurs when unsaturated lipids, stored in water at physiological temperatures, show the effects of oxidation in as little as 72 hours.
The photosensitized oxidation has significance in a broad range of areas, from DNA damage, photodynamic therapy (PDT) of cancer, to polymer science [26]. In the next sections we will treat the photo-oxidation.

Photoproduction of single oxygen

The photosensitized generation of $^1O_2$ is a simple and controllable metod that requires only oxygen, light of an appropriate wavelength, and a photosensitizer (PS) capable of absorbing and using that energy to excite oxygen to its singlet state.
A PS is a molecule that can produce chemical changes in another molecule via a photochemical process. Some types of PSs are: organic dyes (used in this experiment) and aromatics, porphyrins, phthalocyanines and related macrocycles, semiconductors and transition metal complexes.
The PS excitation is achieved through a one-photon transition ($h\nu$) between the ground state S_0 and a singlet excited state S_n. Relaxation of the S_n state yields the lowest excited state of the sensitizer S_1.
The absorption of a photon of energy $h\nu$ brings the PS to an excited state ${S_1}^*$ without changing its spin. By internal conversion, the molecule goes down to its first singlet excited state S_1. Then, there are two possibilities for the PS, either decay to the ground state with the emission of a photon with a low energy, a process called fluorescence with characteristic times $10^{-9} - 10^{-8}$s, or intersystem crossing that brings the PS to a more stable state T_1, the triplet state, with an increased lifetime of about 10^{-4} to 1s.
The lifetime of the state T_1 allows this excited state to react in one of two ways, defined as Type I and Type II mechanisms (figure 3.8).

- Type I mechanism involves hydrogen-atom abstraction or electron-transfer between the excited sensitizer and a substrate, yielding free radicals. These radicals can react with oxygen to form an active oxygen species such as superoxyde radical anions.

- Type II mechanism can be described by the following scheme:

$$PS(S_0) \xrightarrow{h\nu} PS(S_1) \xrightarrow{k_{ISC}} PS(T_1)$$

$$PS(T_1) + {}^3O_2 \xrightarrow{k_{en}} PS(S_0) + {}^1O_2$$

where PS, photosensitizer; S_0, singlet ground state; S_1, first excited singlet state; T_1, first excited triplet state; k_{ISC}, rate constant of intersystem crossing; k_{en}, rate constant of energy transfer; $^3O_2$, ground state of triplet oxygen; and $^1O_2$, singlet oxygen.

Each PS molecule can typically produce $10^3 - 10^5$ molecules of $^1O_2$ before being degraded through photobleaching by $^1O_2$ [26]. These processes are illustrated in the Jablonski diagram in figure 3.8.

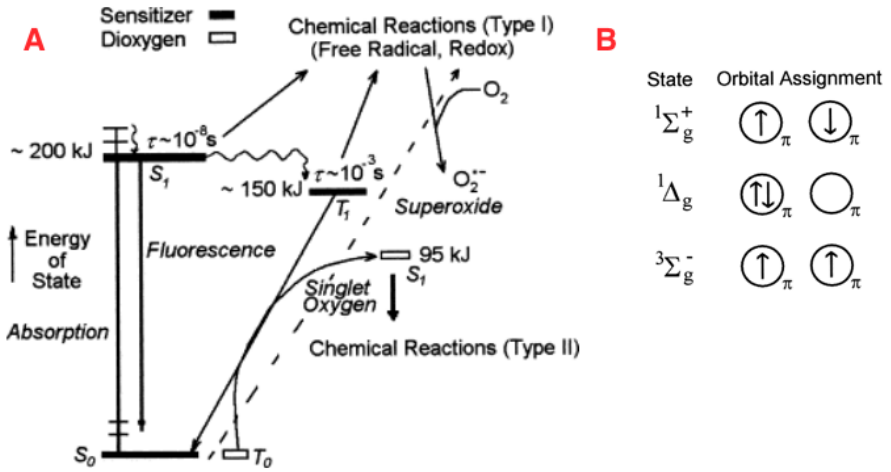

Figure 3.8: **A** generation of excited photosensitizer states and reactive dioxygen species **B** Primitive representations of molecular oxygen singlet and triplet states [26].

Now that the process is clear, it can be understood why the PSs should exhibit the following properties:

- high absorption coefficient in the spectral region of excitation light
- a triplet state of appropriate energy ($E_T \geq 95\ kJmol^{-1}$) (to allow for efficient energy transfer to oxygen in the ground state)
- high quantum yield of the triplet state ($\Phi_T \leq 0.4$) and long triplet state lifetimes ($\tau_T > 1\ \mu s$) since the efficiency of the photosensitizer is dependent on the photophysical properties of its lowest excited triplet state
- high photostability [26].

high levels of oxidation lead to membrane degradation. In particular, the amount that a lipid bilayer vesicle can withstand before collapse depends on the composition of the membrane [58].

Chapter 4

Phase Separation in GUVs induced by light

4.1 Introduction

Lipid bilayer membranes undergo a complex physical behaviour. Membranes containing multiple lipid components can laterally separate into coexisting liquid phases that have a distinct composition. These two phases phases are called liquid-ordered L_o and liquid-disordered L_d, or liquid crystalline[1], phase for the degree of order of their acyl chains.
A membrane made of a ternary mixture of lipids of different transition temperatures exhibits different behaviour depending on the temperature of the external bath where it is immersed. At high temperature the membrane is uniform because all lipids in the bilayer mix uniformly in a single liquid phase. But as the temperature is lowered, a transition occurs and the membrane undergoes a phase separation. After that, the membrane contains domains of a phase whose lipid composition differs from that of surrounding phase [51].
Since the first descriptions of this phenomenon by Dietrich et al. [60] and Samsonov et al. [61] the understanding of the underlying physical chemistry of fluid bilayer phase coexistence has considerably progressed. Temperature dependence of lipid mixing-demixing transitions have been investigated extensively [14]. The composition and phase-partitioning dependence of lipid fluorophore diffusion as well fluid domain diffusion have been analysed [12, 15, 24].
We adopted a new cutting-edge technique to obtain the phase separation in membranes using light. While in the previous method the composition was kept constant and the temperature was changed, in our technique we kept the temperature constant but we varied the composition. The chemical process that allows this is called *photo-oxidation*, and involves the use of a dye that labels the lipid as a *photosensitizer* (PS). The PS interacts with the oxygen generating a photosensitised singlet oxygen that oxidates the lipid membrane. The new types of oxidised lipids go in different phases than the original ones. By varying the ratio between the lipids that go in different phases it is possible to reach the miscibility point, and in this way to visualise all of the process of phase separation happening for one membrane bilayer

[1]The liquid crystal state is a distinct phase of matter observed between the crystalline (solid) and isotropic (liquid) states. An in depth study of liquid crystals, also including lipid bilayers, was carried out by De Gennes [59]

at a time.

4.2 Materials and Methods

4.2.1 Preparation of Giant Unilamellar Vesicles

We studied Giant Unilamellar Vesicles (GUVs) fromed from a ternary mixture of lipids. The preparation of GUVs was carried out by standard electroswelling method described by Angelova et al. [6].
Lipid mixtures were prepared with different lipids at different concentrations according to the experiments. All the lipids are obtained from Avanti Polar Lipids (Alabaster, AL). The fluorescent probe Rho-1,2-dioleoyl-sn-glycero-3-phosphoethanolamine (DOPE) was added.
A small quantity of lipid mixture dissolved in chloroform was deposited as a thin film on the surfaces of two conductive glasses (coated with Indium Tin Oxide), the ITO glasses. The glasses were placed in a desiccator for at least two hours to remove any traces of chloroform from the lipid film. They were mounted with their conductive sides facing each other in a Teflon chamber and separated by a spacer also in Teflon (figure 4.1 A). The electroswelling chamber was filled with a 0.103 osmol/kg sucrose solution. The glass plates were connected to a function generator and an alternating voltage of 4 V peak-peak with a 10 Hz frequency was applied for 2 hours (figure 4.1 B). The vesicles solution was removed from the chamber and put in a bottle washed before with 6g/l Bovine Serum Albumin (BSA).
The osmolality was measured with a cryoscopic osmometer. The accuracy of the measurements is 0.001 osmol/kg. Independent preparations were prepared for every specific composition.

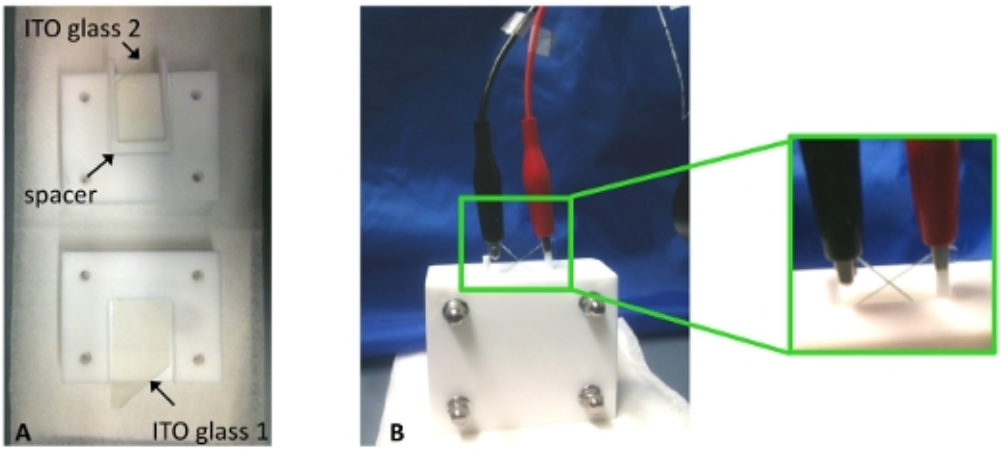

Figure 4.1: **A** Electroswelling chamber with two ITO glasses and spacer. **B** Electrodes connected to ITO glasses.

4.2.2 Materials

In the following table the lipids and the fluorescent probes, that were used during experiments, are listed.

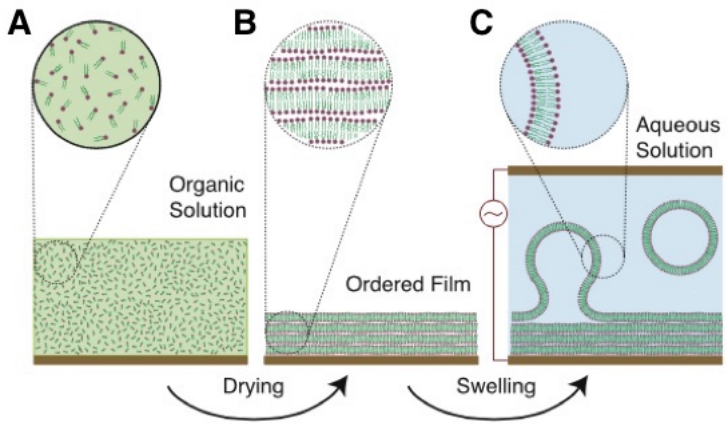

Figure 4.2: Three steps of electroformation. From the left: **A** Lipids are dissolved in an organic solvent and **B** dried on the plates of a capacitor. **C** The space between the plates is filled with an aqueous buffer and an oscillating electric field is applied. On timescale of hours the electric field causes vesicles to swell from the lipid film and continue to grow by fusion.

Acronym	Name
POPC	1-palmitoyl-2-oleoyl-sn-glycero-3-phosphocholine
DOPC	1,2-Dioleoyl-sn-glycero-3-phosphocholine
DLPC	1,2-dilauroyl-sn-glycero-3-phosphocholine
SM	Brain Sphingomyelin
DOPE-Rhod	1,2-Dioleoyl-sn-Glycero-3-Phosphoethanolamine-Rhodamine
Chol	Cholesterol

Table 4.1: Lipids used during the experiments. They were purchased from Avanti Polar Lipids (Alabaster, AL)

The dyes Alexa 674, Perylene, DiD, Dil, Fm4-64 were purchased from Life Technologies.

4.2.3 Optical microscopy observation and irradiation

Observation of GUVs was performed under an inverted microscope Axiovert 200 (Carl Zeiss, Oberkochen, Germany) equipped with a 100x oil immersion objective (NA=1.4, Zeiss). Images were taken with a CMOS camera (Hamamatsu Orca Flash 40V2). Irradiation of the DOPE-Rhodamine was done using 561 nm laser Coherent Sapphire 561 CW CDRH. The intensity of the irradiation was 1.4 kW/cm^2, measured with a powermeter. The optical scheme of the setup is reported in figure 4.3.

4.3 Results and Discussion

The starting point of this experiment was to choose *the right composition* for the GUVs that allows to observe the phenomenon we are interested in. Since we want to induce phase separation we prepared the GUVs at a composition that is not critical.

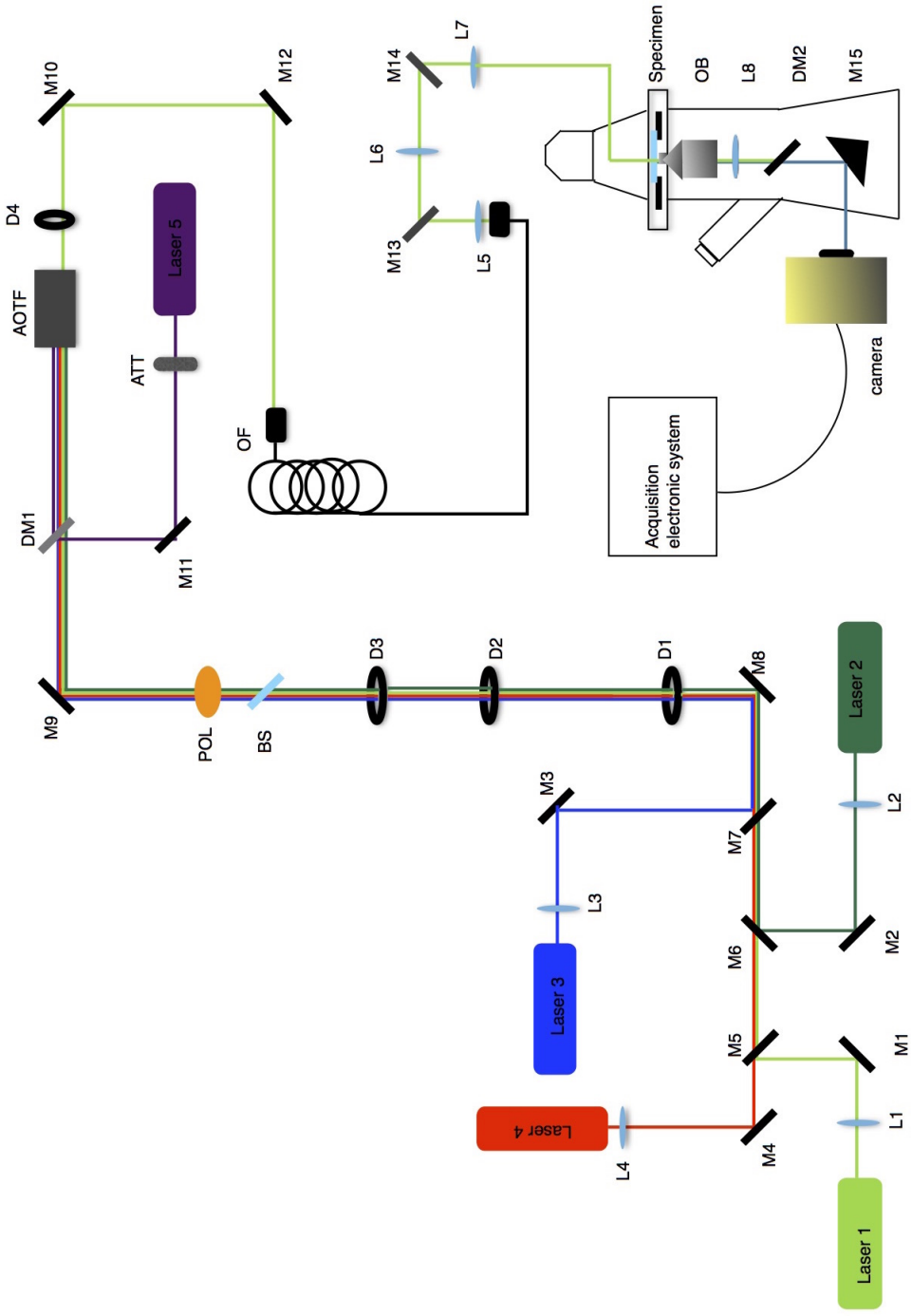

Figure 4.3: **Single molecule fluorescence microscope** Five lasers (405 nm , 488 nm, 514 nm, 561 nm, 639 nm) are focused on the backfocal plane of a high NA 100x oil objective which results in epi wide field illumination of the sample. The lasers 488 nm, 514 nm and 561 nm are Optically Pumped Semiconductor Lasers (OPSL). The lasers 639 nm and 405 nm are Diode Pumped Solid State lasers (DPSS). The fluorescence light is split by a dichroic wedge and directed to the CMOS camera (Hamamatsu Orca Flash 4 V2). The wavelength and excitation timing is controlled by an acousto-optical filter (AA-OptoElectronic, AOTFnC-VIS). The pixel size is 69.3 nm.

Furthermore, because the dye suffers photobleaching it is not possible to change a large quantity of lipids without compromising the imaging of the process. Therefore, we needed to prepare the GUVs with a composition that is outside the critical coexistence region, but not too far from that.
To date, there are no ternary phase diagrams for all lipid mixtures. Nevertheless, in a previous study [29] an attempt to draw the critical line for some mixtures was performed. The starting conditions for our lipid mixtures are based on this work.
We employed different lipid mixtures to be able to see the entire process of the phase separation. In figure 4.4-4.5 there are several ternary plots with the employed compositions.
It is important to note that artificially produced GUVs from a mixture do not *all* have the *same* concentration, it can differ from one to another [50].

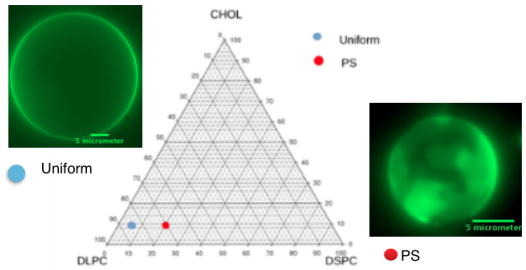

Figure 4.4: Ternary plot for a mixture of Chol DLPC and DSPC. Every point corresponds to an experiment. Images of a uniform GUV (left) and a phase separated GUV. The bar scale is 5 μ.

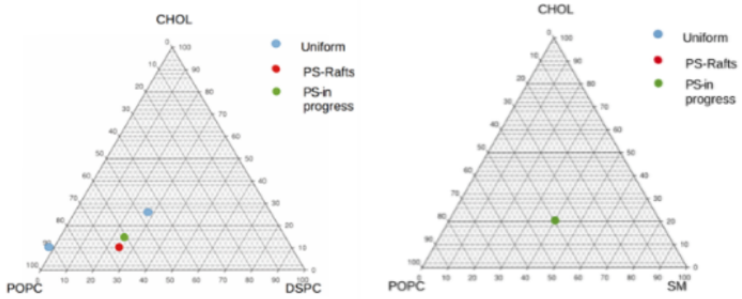

Figure 4.5: Ternary plots for POPC,DSPC,Chol and POPC,SM,Chol mixtures. Every point corresponds to an experiment. GUVs exhibit light-induced domain separation for mixtures of POPC:DSPC:Chol=60:25:15 and POPC:SM:Chol=40:40:20.

In all the experiments that will be described in this thesis it a lipid mixture made of 40% POPC, 40% SM and 20% Chol (Mass percentages)[2] was employed . In addition, we used the fluorescent lipid DOPE-Rhod. This has a strong preference for

[2]More than ten independent preparations were produced

the L_d phase, like POPC , therefore the final composition was: 35% POPC, 40% SM, 20%Chol and 5%DOPE-Rhod. The recipe is reported in Appendix A7.3 (recipe 1). To choose the quantity of dye, several factors were kept in mind. Firstly, the number of dye molecules is proportional to the number of lipid molecules that can be photo-oxididated, and secondly, there should be enough dye to both induce and image the process of the phase separation before the dye is completely bleached.
Once the GUVs were prepared at the composition described earlier, they were observed under the microscope.
During the irradiation a quantity of the lipids that go in the L_d phase (POPC and Chol) are converted in lipids that go in the L_o phase via the mechanism of photo-oxidation that is described in Section 3.2. When a critical composition is reached, the lipid membrane separates in different phases.
Even though we do not exactly know the final structures obtained after the conversion for the photo-oxidized lipids, some hypotheses were proposed [27]. In figure 4.6 we have reported the structures of the results of the photo-oxidation reaction of POPC and Cholesterol. The structures of the lipid oxidized show a kink and a peroxide group in one of the tails (inset figure 4.7)
A scheme of the performed experiment is presented in figure 4.7.

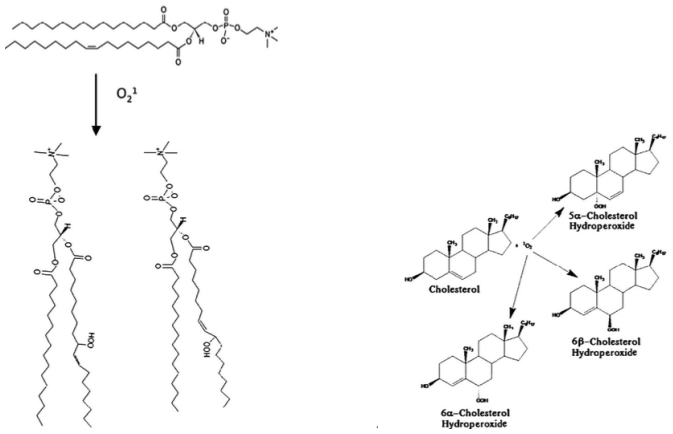

Figure 4.6: Molecular structures of the hydroperoxides formed during the photo-oxidation reaction of POPC and Cholesterol via singlet oxygen.

The initial composition with which the GUVs are prepared ensures that they are all uniform, even at low temperatures. Upon irradiation, a part of the membrane is photo-oxidized and the ratio between liquid ordered and disordered lipids increases resulting in a movement through the phase diagram, as shown with a red arrow in figure 4.7. Once the quantity of lipids converted is enough to enter the two-phase coexistence region, the GUVs undergo a phase transition and liquid ordered domains begin to appear. It is important to make clear that one important advantage of this technique is that it is possible to induce the phase separation of a single GUV, instead of all the sample at the same moment as an experiment in which the temperature is decreased to achieve phase separation.

The sequence of phase separation induced by light of a single GUV is reported in figure 4.8. The equatorial plane of the GUV is imaged during the process.
GUVs made from the lipid mixture described in the recipe 1 (Appendix A7.3) does not show phase separation at room temperature. Indeed at the time t = 0 s the GUV

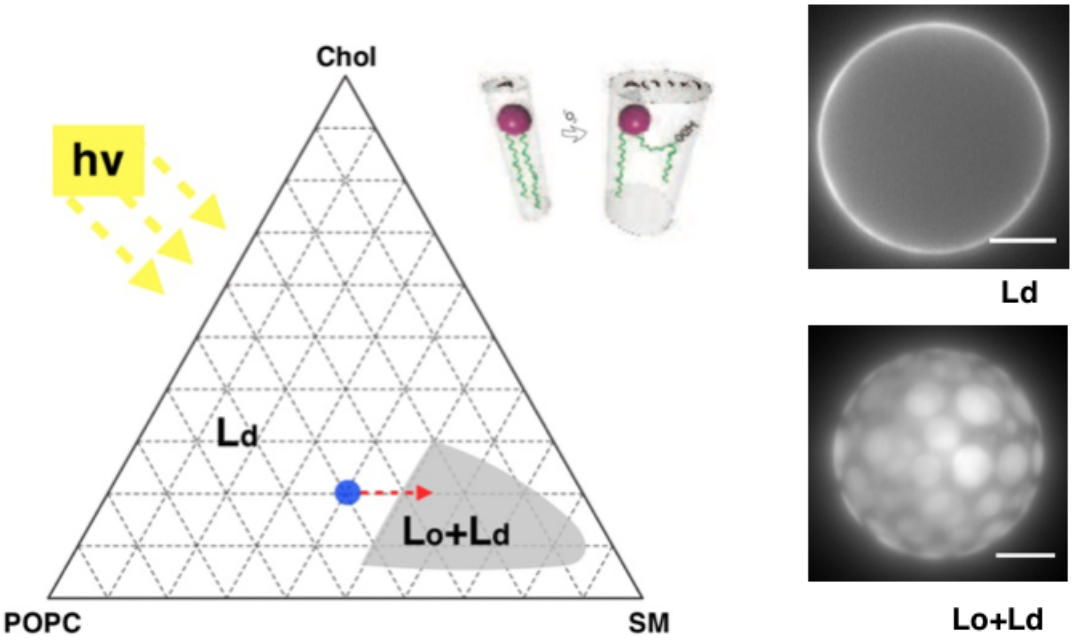

Figure 4.7: **Phase diagram of 3-component lipid bilayer (POPC, SM, Chol)** Representation of the experiment carried out: the blue dot outlines the *starting composition*. The phase coexistence region is shown in gray. The red arrow follows the composition of a GUV under irradiation, varying throughout the experiment. In the inset a sketch of the photo-oxidation of a single lipid molecule is drawn. The oxidized molecule exhibits a *kink* in one of the tails. On the right, an example of a GUV in the L_d phase, with a composition represented by the blue dot, and another in $L_o + L_d$ phase, with a composition inside the gray region.

is uniform and its composition is approximately the one described above. Thermal fluctuations of the order of k_BT are present. After some seconds of irradiation, the effects of the photo-oxidation are already visible. The GUV starts to fluctuate such that morphological changes of its shape can be observed. After the deviation from the initial circular shape is visible. Even though we cannot measure the composition of the GUV at this point, we know that a number of lipid molecules are oxidized and the presence of these large fluctuations suggests that the composition is near the critical coexistence region. We paid particular attention to these fluctuations,which are futher analysed.
Once the border of the critical region is crossed, the GUV shows the presence of L_o domains in the surrounding L_d phase. It is important to highlight that the GUV at this point recovers its initial circular shape and from this time to t=30 s the arrangement of the domains is symmetrical, minimizing the interaction energy between the two phases.

4.3.1 Shape deformations and area increasing

When the composition of the GUVs is near the critical composition, the GUVs exhibit shape fluctuations that are visible by eye through a microscope. In figure 4.9 is drawn what happens on a GUV under irradiation and in figure 4.10 we reported an example of what was observed during experiments.

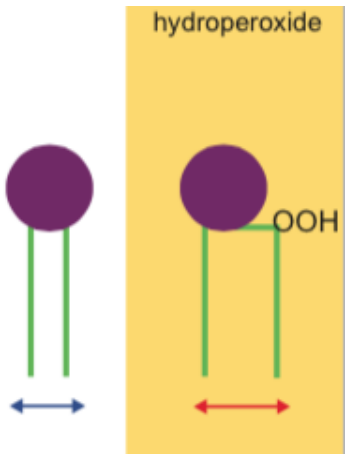

Figure 4.11: Scheme of the structure of oxidized lipids. The area of the oxidized molecule is bigger than the original one [64].

The *driving force* that underlies the presence of these fluctuations is the variation of the surface area of the GUVs, caused by photo oxidation. It is a *chemical force*. The area of the GUVs grow during the irradiation because the oxidized lipids have a different structure and occupy a larger area than the original lipids (figure 4.11). Previous studies [64] suggest that the larger conformation of the oxidized lipids is due to a hydrophillic group close to the position of the initial unsaturation that migrates towards the water surface to minimize the energy. We can define the total variation of the area of the GUVs as:

$$\Delta A = N \cdot \delta a$$

where N is the number of oxidized lipids and δa is the area variation for single oxidized lipid molecule . A first attempt to determine the value of δa for 1-palmitoyl-2-linoleoyl-sn-glycero-3-phosphatidylcholine (PLPC) was carried out using simulations [65], but further chemical studies are required.
We estimated the macroscopic variation of the area for the GUVs. To do this, we calculated the contourlength of the GUVs at every frame employing the algorithm described in Section 4.3.2 The area of the GUVs is proportional to L^2, the square of the contourlength.

In figure 4.12 we reported the variation of L^2 for a GUV that was irradiated for

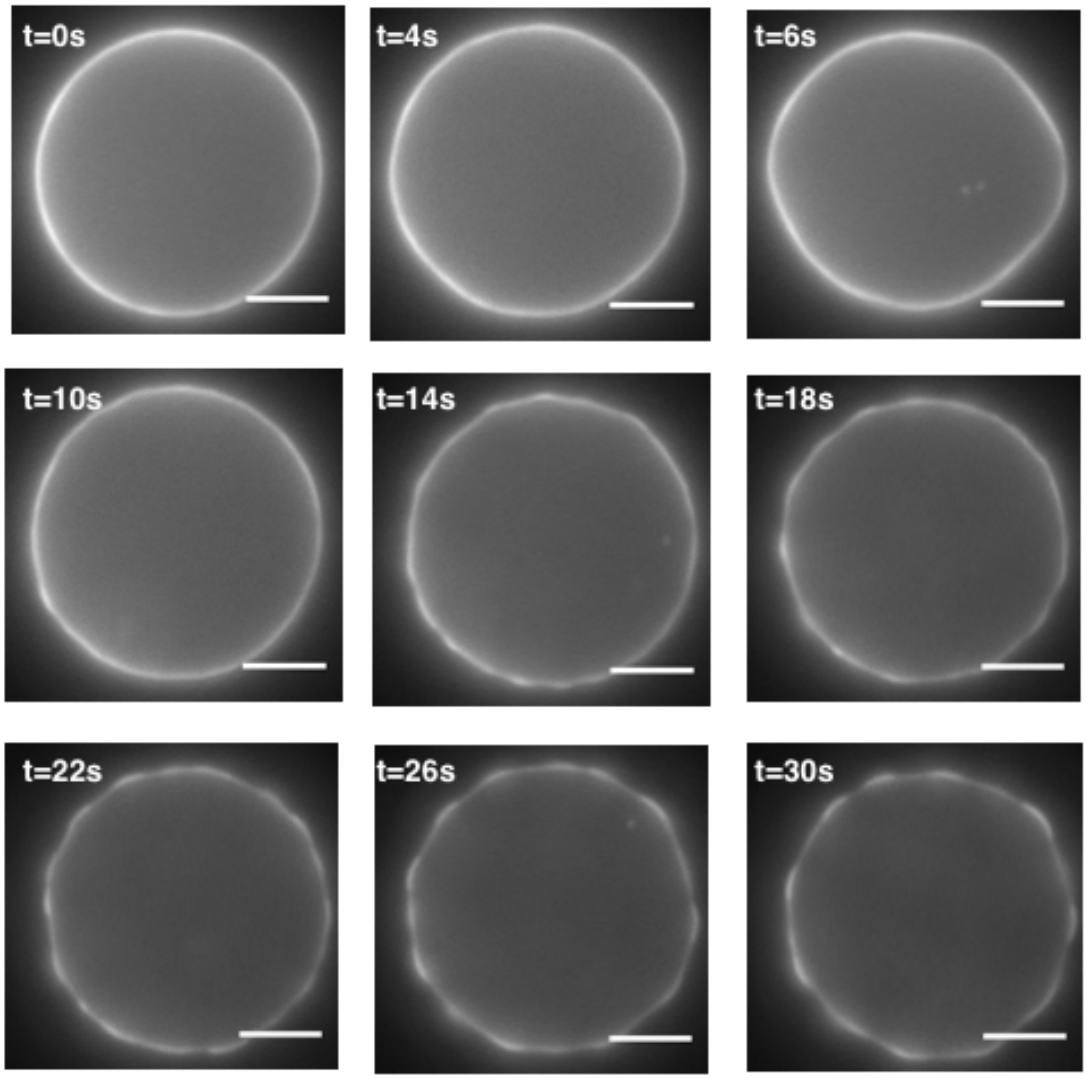

Figure 4.8: **Sequence of images of one GUV during phase separation.** The scalebar is 5 μm.

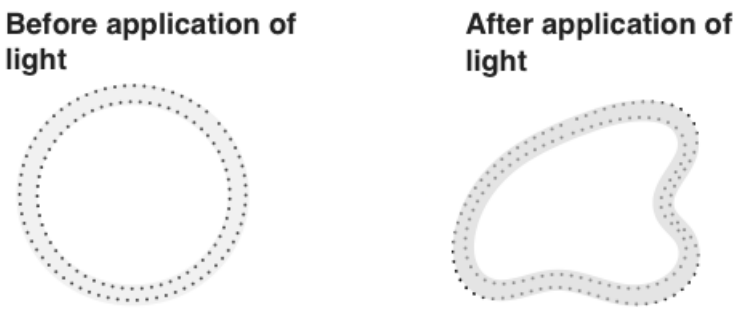

Figure 4.9: Sketch of the behaviour of a GUV before and after irradiation

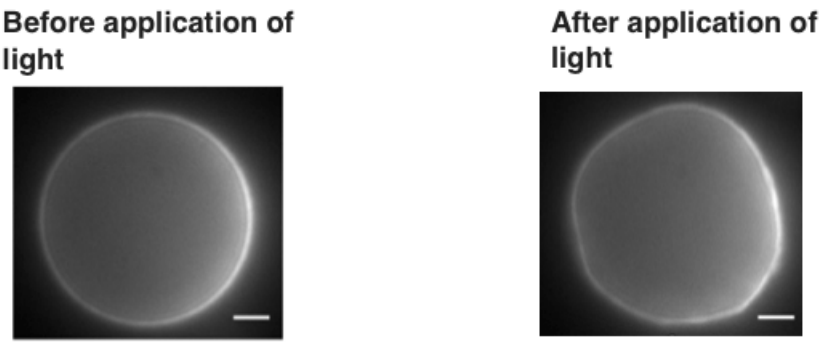

Figure 4.10: Example of a GUV before and after irradiation. The scalebar is 5 μm .

50 s and showed phase separation. Analysis of ten GUVs showed an average increase of the area of 16% during photo-oxidation.

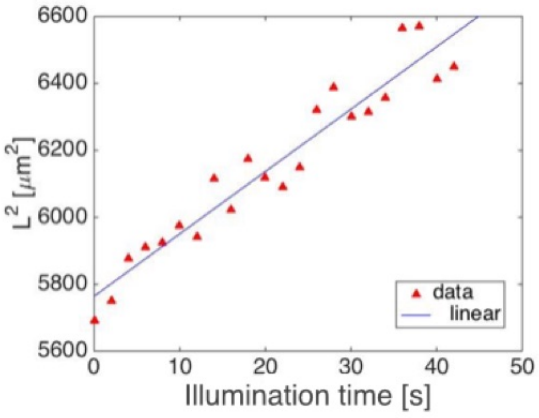

Figure 4.12: Variation of L^2 as a function of time.

4.3.2 Fluctuations as signature of a non equilibrium process

Here we present the study of the fluctuations of a group of GUVs that undergo phase separation with two independent analyses conducted using custom scripts written in MATLAB [66].
In the first analysis we examined the fluctuations of the shape of the vesicles and in the second the fluctuations of the composition.
For both the studies we determined the correlation function of the fluctuations before the phase separation, at the transition and after the phase separation.
In the first analysis we calculated the shape fluctuations of the GUVs and their Fourier spectra. From that analysis we obtained the behaviour of the surface tension and the bending modulus of the GUVs near critical point. In the second analysis we studied the behaviour during the phase transition using a correlation function
It is noteworthy that this is an experimental analysis of the process, that can hopefully provide a basis for a theoretical model of the phenomenon.

Shape fluctuations

The raw data of a typical vesicle imaged from the equatorial plane are shown in figure 4.13 A. The lateral resolution of the equatorial optical section was limited by diffraction and pixelation effects. In the normal direction, a high (subpixel) accuracy was obtained. In figure 4.13 B we reported a typical intensity profile along a line perpendicular to the contour.

Each peak corresponds to the position of the GUV membrane. We determined the position fitting the intensity peaks along the edge of the GUV with the Gaussian function. The positional accuracy achieved was about 20 nm.
We calculated the edge of the vesicle for every frame. Once obtained it (figure 4.14 A), the fluctuation spectrum in the *real space* was calculated. To do this, we divided the contour in a finite number (usually about 1200) pieces denoted by the position s (figure 4.14 B). We calculated the centre and the radius R of a circle that fitted the GUV. We then define the shape fluctuations as the difference between the the local radius r of the patches s and the mean radius R:

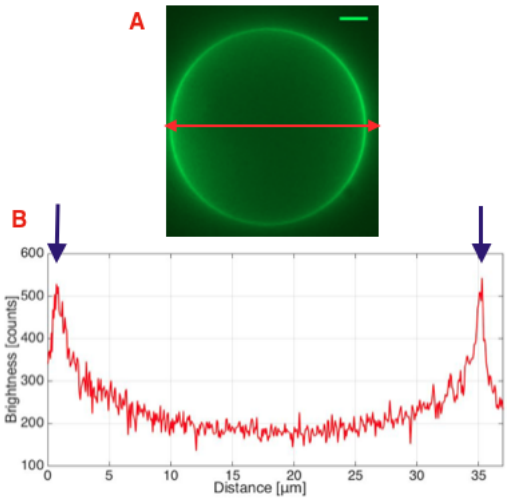

Figure 4.13: **A** Equatorial plane of a GUV. The scalebar is 5 μm. **B** Intensity profile normal to the vesicle contour. The peaks represent two points at the edge of the GUV.

$$u(s) = r(s) - R$$

In figure 4.15 an example of a fluctuation spectrum in real space is shown. The Fourier transform of the spectrum is obtained from

$$u_k = \frac{1}{a}\int_{-\frac{a}{2}}^{+\frac{a}{2}} r(s)e^{-ik\cdot s}ds$$

where a is the arclength of the contour patch and $k = n \cdot \frac{2\pi}{a}$ with n a non-zero integer.

The algorithm we used does not only calculate the experimental Fourier spectrum from fluctuations, but also fits it with a theoretical model [12]. This allows to extract the values of the surface tension and the bending modulus, which are two of the parameters in the fit. Briefly, the model was obtained from the Canham-helfrich free energy for a flat membrane. Correction for the spherical shape of the GUV and the averaging of the fluctuations during the camera illumination time were included. The final expression for the model is given by:

$$\overline{<|u_k|^2>} = \sum_{q_k}\left(\frac{sin((k-q_x)\frac{a}{2})}{(k-q_x)\frac{a}{2}}\right)^2 \cdot \frac{L}{2\pi}\int_{-\infty}^{+\infty} dq_y \frac{k_BT}{L^2 2\eta q}\tau_q\frac{\tau_q^2}{t^2}\left(\frac{t}{\tau_q} + e^{-\frac{t}{\tau_q}} - 1\right)$$

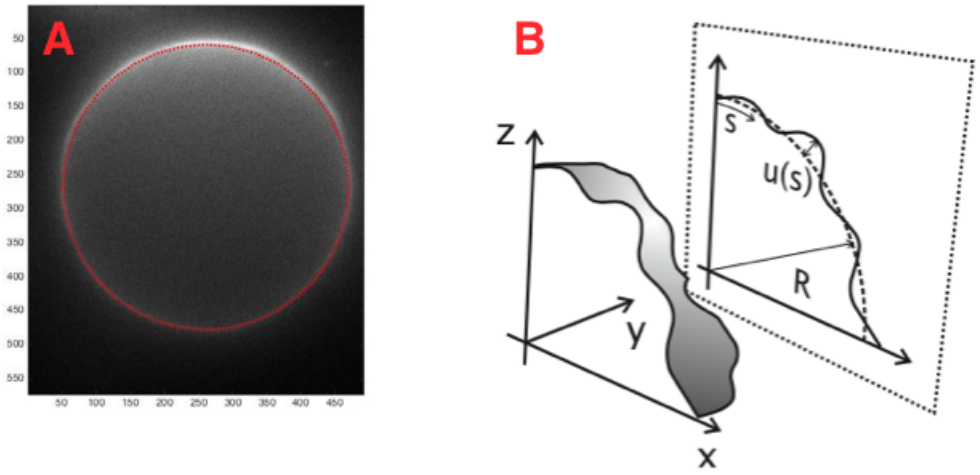

Figure 4.14: **A** Equatorial plane of a GUV. The contourlength is drawn in red. **B** Optical section along the equatorial plane. For the arclength s the deviation from the mean radius R is u(s).

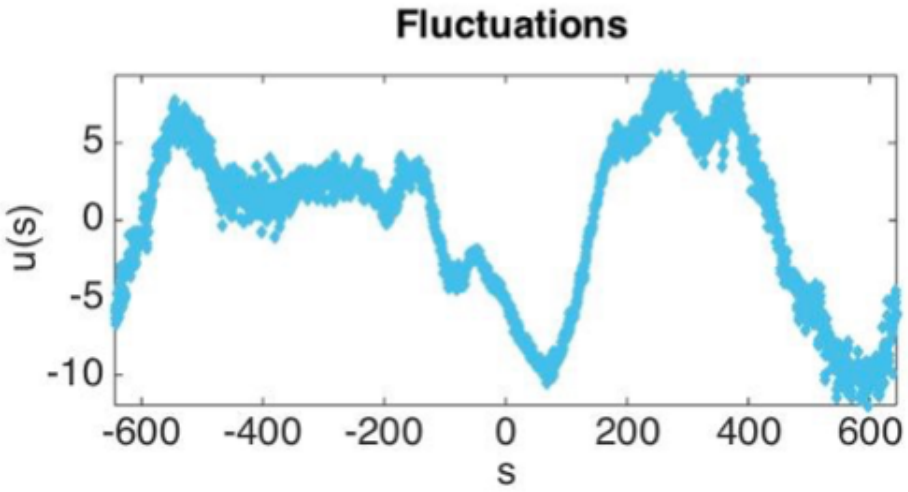

Figure 4.15: Example of a fluctuation spectrum in real space

where

$$\tau_q = \frac{4\eta q}{\sigma q^2 + \kappa q^2}$$

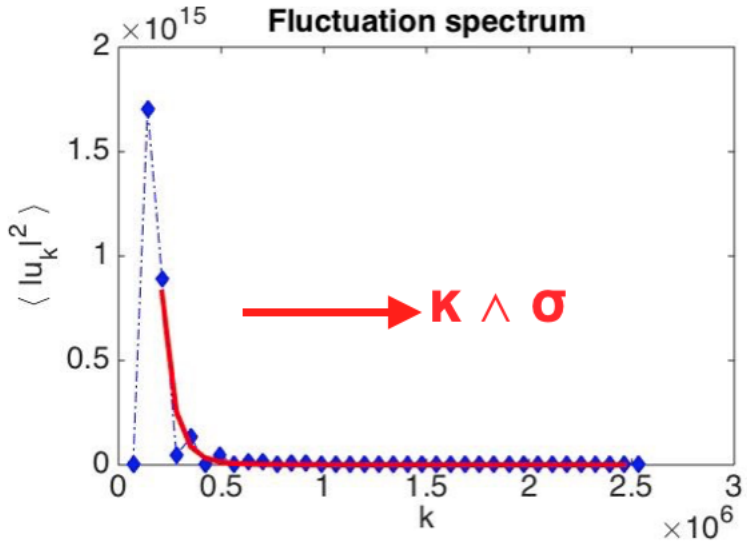

Figure 4.16: Example of a fluctuation spectrum in Fourier space.

It is important to underline the presence of σ, the surface tension, and κ, the bending modulus, that can be extracted from the fit as independent parameters (figure 4.16)

We analysed the time evolution of the shape fluctuations in the real space for GUVs calculating the spectrum for every frame. In figure 4.17 and 4.18 spectra of one GUV[3] are reported at different times.
At t=0 s the GUV exhibits fluctuations with amplitude of the order of the thermal fluctuations. After seconds of irradiation the shape of the GUV starts to be deformed such that the fluctuation amplitude is more than 10 times bigger than at t=0 s. It is interesting to note that the amplitude of fluctuations increase until the moment of phase separation. When the vesicle is phase-separated the fluctuations become smaller and the vesicle becomes spherical again. What we see in the last spectrum of figure 4.18 are not the fluctuations, but the domains of the L_d phase that bud out. In figure 4.19 is shown the time dependence of the standard deviation of the fluctuation spectra.

[3]It is the GUV in figure 4.8. See that image.

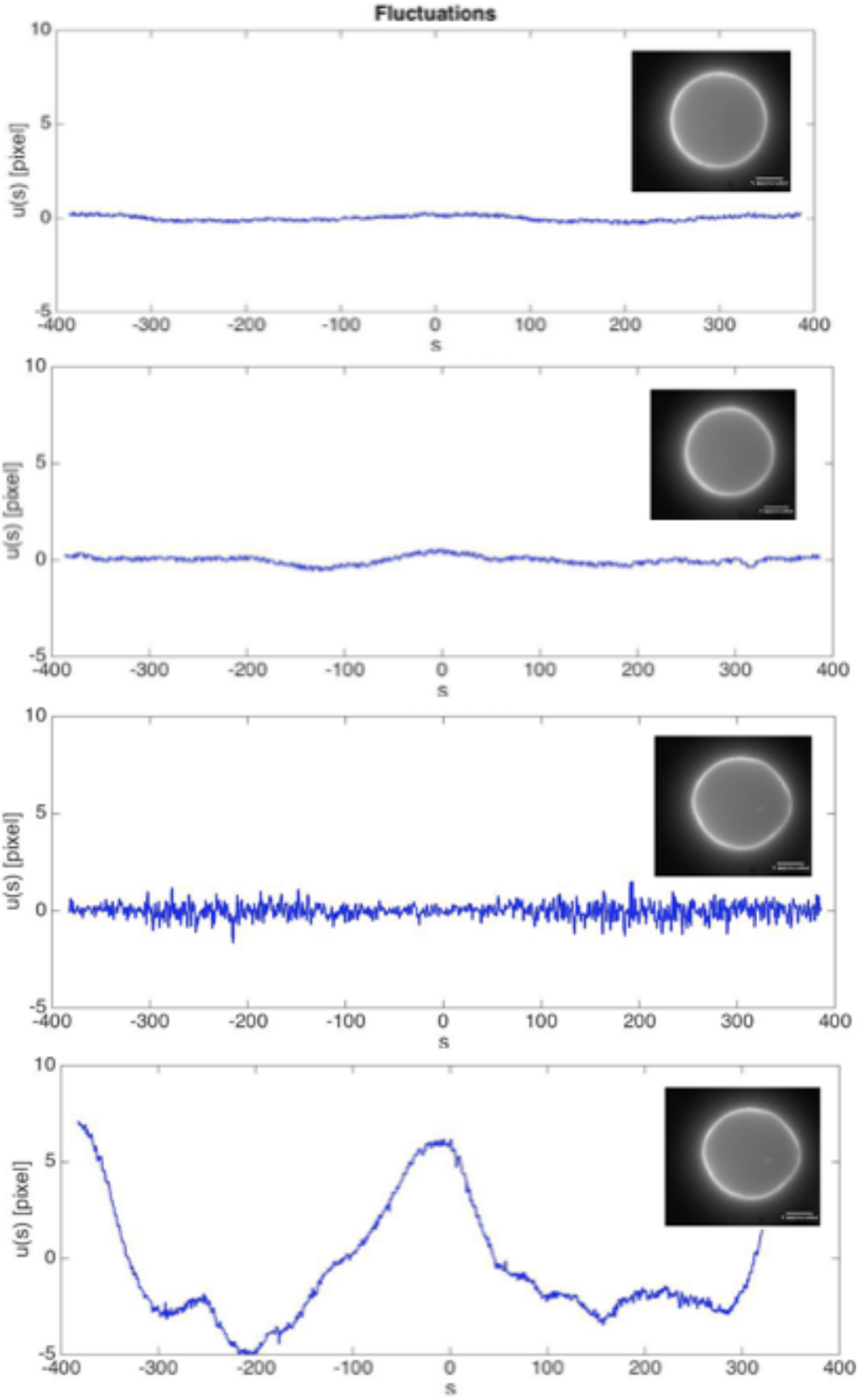

Figure 4.17: Fluctuation spectra in real space. The insets show the images of the GUV from which the spectra are calculated. From the top to the bottom the images are taken at time: t=0 s,t=2 s, t=4 s, t=6 s

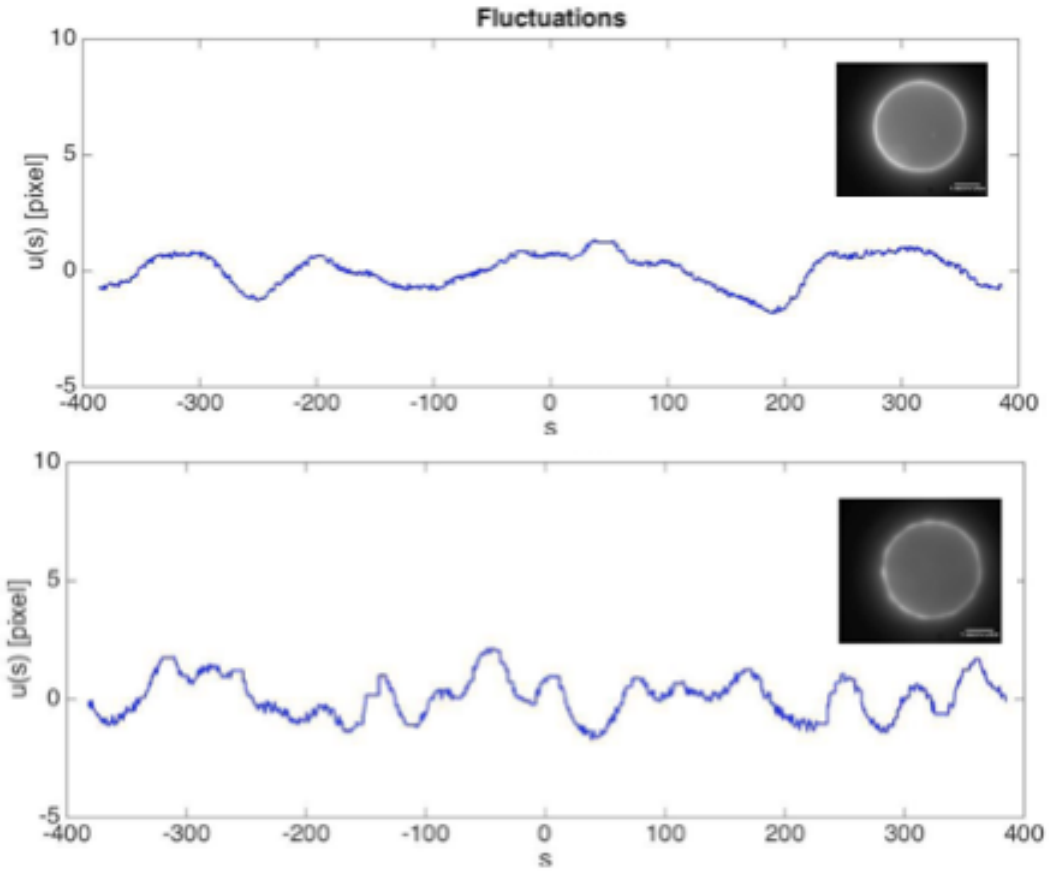

Figure 4.18: Fluctuation spectra in real space. IThe insets show the images of the GUV from which the spectra are calculated. From the top to the bottom the images are taken at time: t=16s, t=22s

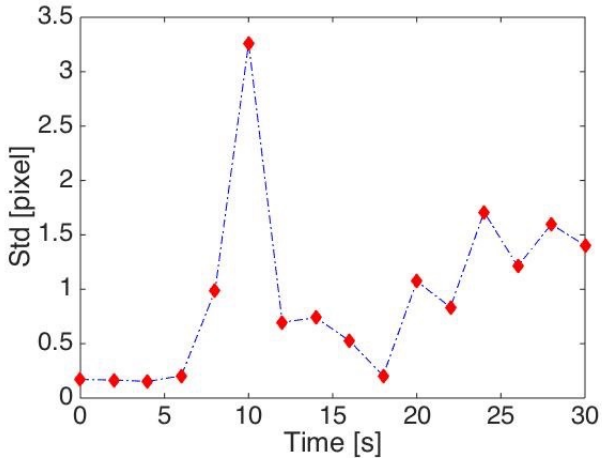

Figure 4.19: Time dependence of the standard deviation of the fluctuation spectra.

By fitting the Fourier spectrum of the fluctuations to our model we get the physical parameters that describe the vesicles: the surface tension σ and the bending modulus κ (figure 4.16). We observed that the surface tension decreases as the shape of the vesicles deformes. In figure 4.20 we can see how the decrease of the surface tension is associated with the increase of the amplitude of the fluctuations.

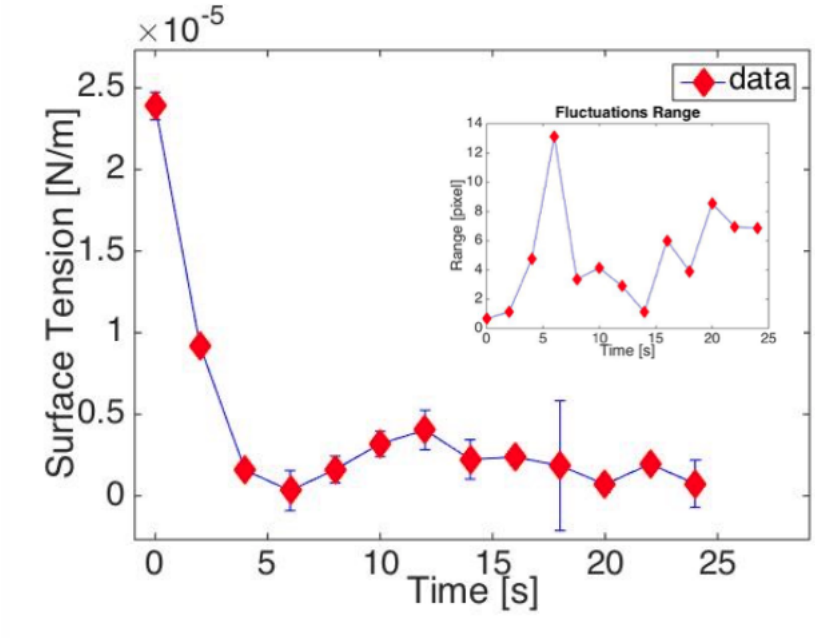

Figure 4.20: Time dependence of the surface tension. In the inset there is the variation of the range of the fluctuations in time.

The fluctuations increase to a maximum value and then decrease. We consider the point where the amplitude starts to decrease as the critical point of the phase transition.
It is interesting to notice that when the fluctuations start to decrease the surface tension reaches a minimum. After the phase separation domains start to appear and aggregate and each different domain has its own surface tension. In our graphs the values in the region that corresponds to the time after the phase separation are an average of the various istantaneous surfaces tensions of the momentary domains. The calculation of the surface tension of the individual domains after the phase separation was not our purpose, nevertheless it would be an interesting analysis to do in the future.
In figure 4.21 we reported the variation of the surface tension during time. Every color corresponds to a different GUV.
When we look at the behaviour of the surface tension, we can deduce that it is one of the possible response functions of the phenomenon.
It is important to specify that in this experiment the time is a measure of the istantaneous composition of the vesicle, since the longer the vesicle is irradiated, the more lipids are oxidized. Therefore the time is an order parameter during transition. In a critical process the the response function has a power law dependence on the order parameter, therefore the critical behaviour of the surface tension is expected

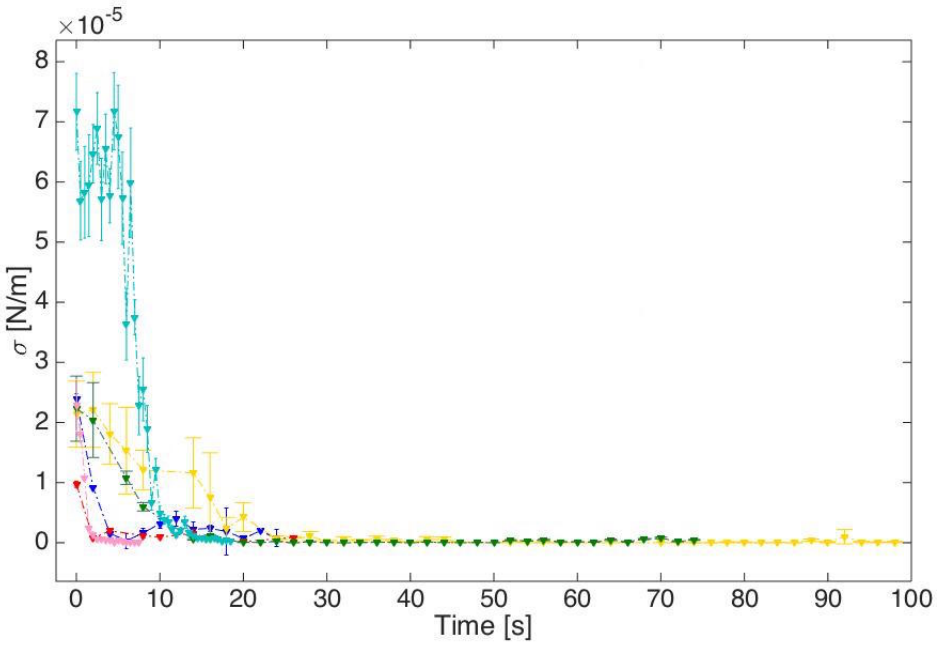

Figure 4.21: Time dependence of the surface tension for a group of GUVs.

to obey:

$$\sigma \approx |t_c - t|^{\nu}$$

with ν a critical exponent and t_c the time at which the transition occurs. If the process is at equilibrium, the law of universality holds for the critical exponent and ν is expected to belong to the 2D Ising universality class.

We fitted the surface tension versus time using a power law, in a log log scale. An example of this fit is shown in figure 4.22. The fit shows a clear power dependence of the surface tension on time, as expected for a critical process. *But is it an equilibrium process?* We answered this question doing three experimental tests. Firstly it was tested if the process was universal.
If we look at the values of the slope ν of the curves in figure 4.23, we can observe that they are different from each other, even considering the error. There is no universality in the process of phase separation induced by light. Therefore the process is not an equilibrium process. The process of phase separation driven by temperature is an equilibrium process, for

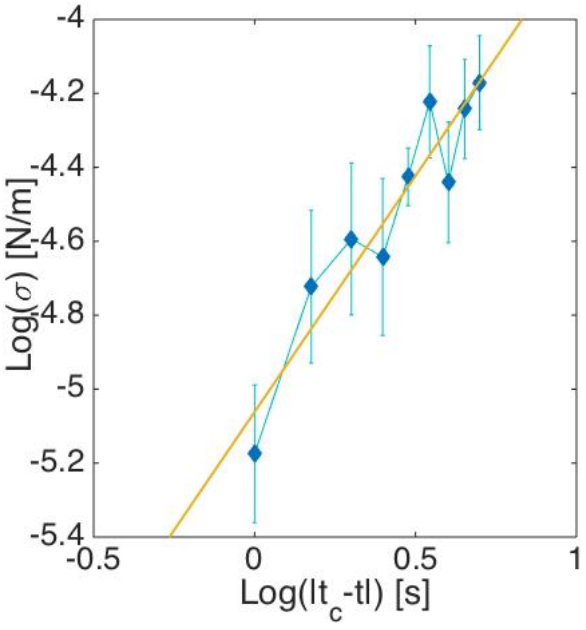

Figure 4.22: Fit of the surface tension of one GUV in a log-log scale.

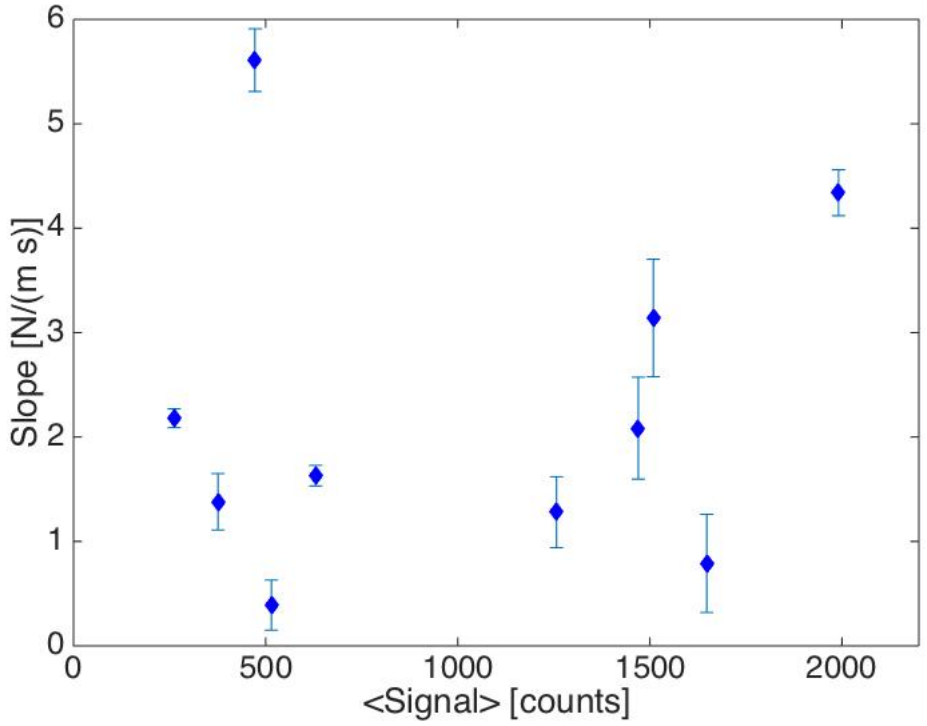

Figure 4.23: Values of the slope m for the GUVs

which the universality is valid. In the
case of phase separation induced by light, a chemical force, that drives the system away from the equilibrium, is introduced. This force is the light. In this situation the evolution of the surface tension can be expressed with:

$$\sigma \approx A \cdot |t_c - t|^{\nu 1} + B \cdot |t_c - t|^{\nu 2} + ...$$

where the first term depends on the physics intrinsic of the vesicle and the second depends on the physics of the photo-oxidation of the vesicle; t is the time and t_c is the critical time, or the time at which the transition occurs.
Secondly it was noticed that the process is irreversible. The structure of lipids is irreparably changed through photo-oxidation. It is not physically possible to return to the initial state when the vesicle is uniform with a chemical reaction. Also here, the difference from the phase separation with temperature, that is a reversible process, arises. Lastly an experimental test was performed: we started the phase separation with light in a vesicle and at a point we turned off the light. After tens of seconds we turned on the light again to see what happened to the vesicle. We observed that the process does not stop when the light is turned off. Indeed, during the process the vesicle is not in an equilibrium state, but far from that and evolves in order to find another equilibrium state. The time dependence of the bending modulus κ was also analysed.
As shown in figure 4.24 the bending modulus is constant during the process.
The value of the bending modulus depends on membrane composition; this means that the variation of the composition during the photo-oxidation is not enough to induce a considerable change of the value of the bending modulus. The value of

the bending modulus is centered in $1.09 \cdot 10^{-19} J$ This value is compatible with the values reported in literature [13].

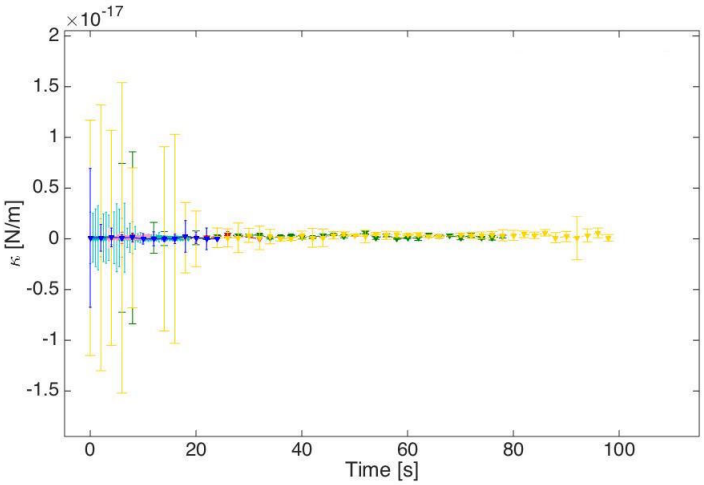

Figure 4.24: Time dependence of the bending modulus for the analysed GUVs.

Correlation function of shape fluctuations

We performed a final calculation based on the fluctuations in real space. We computed the correlation function of the fluctuations for every frame. If we define the fluctuations as $u(\theta)$ where θ is the angle in the polar coordinates of the point considered, the correlation function becomes:

$$G(\theta) = \frac{< u(\theta_i)u(\theta_i + \theta_{i+j}) > - < u(\theta_i) >< u(\theta_i + \theta_{i+j}) >}{< u(\theta_i)^2 >}$$

The result is plotted in figure 4.25. The correlation function is symmetric as expected from the definition. Since the correlation function of a periodic function has the same period of the function, we are not surprised that at the beginning when the vesicle is uniform the correlation function is the correlation function of a circle. The shape of the curve depends on the polarization of light. Without the polarization, the correlation function of a circle is equal to one everywhere. When the vesicle starts to fluctuate, the correlation function deforms from its initial shape.
At the origin the correlations have the higher values in both cases that is, there is a high correlation between the fluctuation at θ_i and θ_{i+1}. As $\Delta\theta$ increases, the correlation functions decay. If we look at the shapes of the functions we can see that the correlation functions before, in the moment of and after the transition decay in different ways. In particular, the correlation function after the phase separation decays quicker and goes to zero for θ that goes to π.
Even though to date there is no wide literature available about correlation function of critical fluctuations in non equilibrium and finite systems like the one analysed, a previous analysis on non equilibrium chemical reactions in a sequence of boxes revealed similar results [68].

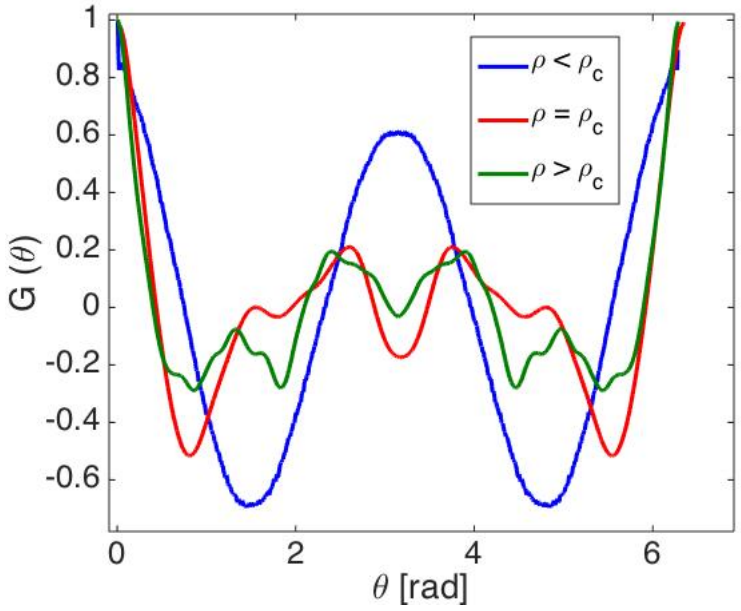

Figure 4.25: Correlation function of the fluctuations at three different times for the GUV1. We indicated ρ_c as the critical composition. When $\rho < \rho_c$ the GUV is at equilibrium, the corresponding G is in blue. The application of the light changes the composition and as the composition is near the critical one, G changes shape. The correlation function at the moment where there is a minimum in the surface tension in figure 4.20 is plotted in red. The correlation function at the end of the phase separation is plotted in green.

Composition fluctuations

We also analysed the the correlation function of the composition. To do this, we studied the brightness along the edge of the vesicles. Since the grayscale intensity of each pixel in an image reports the average membrane composition inside that pixel, we calculated the fluctuations of the lipid composition of the vesicles with the function:

$$G(\theta) = \frac{< I(\theta_i)I(\theta_i + \theta_{i+j}) > - < I(\theta_i) >< I(\theta_i + \theta_{i+j}) >}{< I(\theta_i)^2 >}$$

where $I(\theta)$ is the image intensity at angle θ. We observed the correlation function for every frame and reported its shape before the phase separation, at the transition and after the phase separation (figure 4.26). The same considerations that are made for the correlation function of the fluctuations are also valid for the this correlation function.
Comparing the different correlation functions of the GUVs, we observed that during the whole process the area subtended by the correlation function decrease. We calculated the integral of the correlation function for every frame for the vesicles for which it was possible (figure 4.27). Indeed a high brightness is needed to perform the calculation of the correlation function of the brightness. We estimated the decrease of the correlation function by linear interpolation (figure 4.28). In table 4.2 the results of the fits are shown.

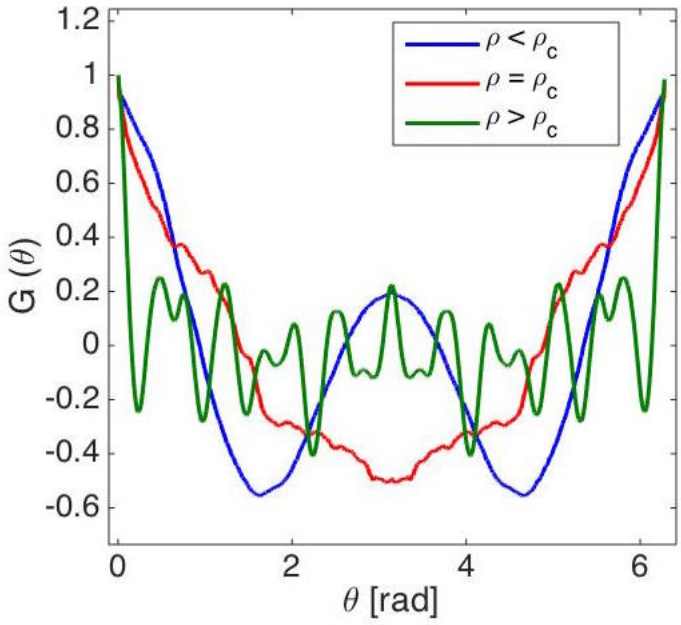

Figure 4.26: Correlation function at three different times for the GUV1. We indicated ρ_c as the critical composition. When $\rho < \rho_c$ the GUV is at equilibrium, the corresponding G is in blue. The application of light changes the composition and as the composition is near the critical, G changes shape. The correlation function at the moment where there is a minimum in the surface tension in figure 4.20 is plotted in red. The correlation function at the end of the phase separation is plotted in green.

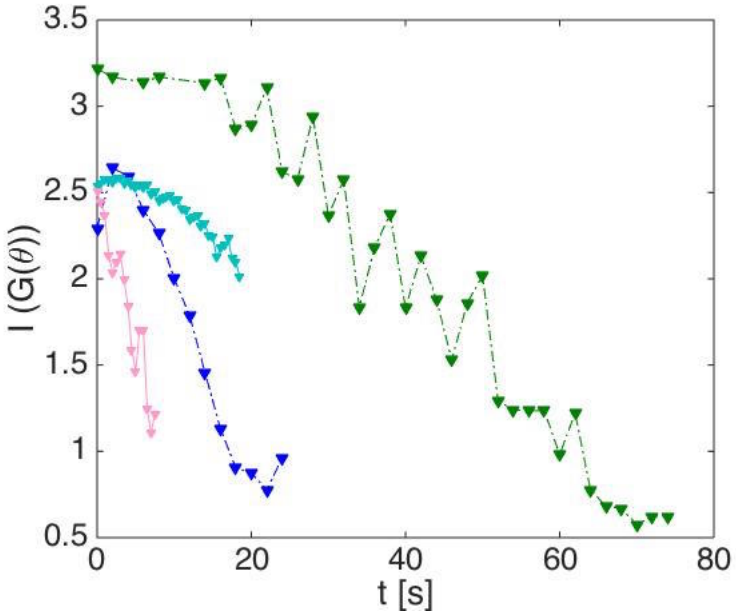

Figure 4.27: Integral of the correlation function G

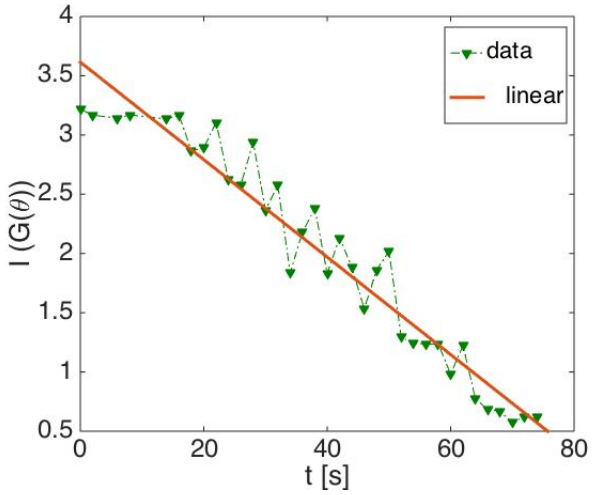

Figure 4.28: Example of one linear interpolation of $I(G(\theta))$.

$y = m \cdot x + q$		
$m\ [s^{-1}]$	q	χ^2
-0.09 ± 0.01	2.74 ± 0.12	0.849
-0.041 ± 0.002	3.61 ± 0.08	0.881
-0.027 ± 0.002	2.66 ± 0.02	0.860
-0.18 ± 0.01	2.52 ± 0.06	0.852

Table 4.2: Fit results of the Integral of the Correlation function.

4.4 Conclusion

We have adopted a new cutting edge technique to obtain phase separation in a controllable way by means of light. The observation of the whole process of phase separation for one vesicle of a time was gained by fine-tuning composition, intensity of light and osmotic pressure. This allowed to see the dynamics of the system near the critical point of the transition, in particular the presence of shape fluctuations. The nature of these fluctuations was analysed. From their quantification, the surface tension and the bending modulus were studied. While the bending modulus is not affected by the transition at the critical point, the surface tension shows a critical behaviour. From universality arguments and experimental tests we concluded that the process of phase separation induced by light is a non-equilibrium process.
The correlation functions of the fluctuations and the composition were analysed. Despite that there is no model available yet, the obtained data would hopefully be the starting point of a further theoretical analysis.

Chapter 5

Receptor compartmentalisation in artificial spines

5.1 Introduction

Experiments with dendritic spines show receptor compartmentalisation in the spine head [8]. Here we investigate one of the possible mechanisms that explain this confinement: the presence of some regions located in the head of spines that hold receptors.
In our lab an artificial system was developed to mimic dendritic spines. We model the head of the dendritic spines with a GUV and use quantum dots as receptors.
In addition we induce phase separation in the GUVs and use the L_o and L_d domains to mimic the confinement regions for receptors. In this way we obtained a simple picture that allows to study how the mechanism of compartmentalisation works.

5.2 Materials and Methods

GUVs were prepared with the protocol described in section 4.2 from a lipid mixture of 40 % SM, 35 % POPC, 5% DOPE Rhod, 20%Chol mass percentages. 16:0 Biotinyl CAP PE (1,2 Dipalmitoyl-sn-Glycero-3Phosphoethanolamine-N) was added to the mixture (Recipe 2, Appendix A7.3).
The solution of quantum dots 705 streptavidin conjiugate (Thermofisher Scientific) and GUVs was prepared immediately before the experiment. 1 μl of quantum dots was diluted in 49 μl of PBS 0.1 Osmol/kg. The solution was centrifuged at 5000xg for 3 minutes. In a Eppendorf tube 500 μl of GUVs solution and 1μl of quantum dots diluted solution were left together for about half a minute. The solution was washed in 1 ml of PBS solution and deposited on a coverslip coated with BSA. Washing the coverslip with BSA was fundamental not only to immmobilise the GUVs on the surface, but also to create conditions on the glass that repel quantum dots, preventing them attaching to the glass.
The sample was irradiated and observed with the setup shown in figure 4.3. We used the 405 nm and the 561 nm laser to image the quantum dots and the GUVs respectively. In order to achieve higher intensity of the 405 nm laser and better observe the quantum dots, the two lenses that expand the beam (L6 and L7) in figure 4.3 were removed. To image the quantum dots and the rhodamine simultaneously

a dichroic wedge was placed in the emission path. This wedge reflects different wavelengths to different locations on the camera.

The trajectories of the quantum dots were followed with an achieved time resolution of 3 to 7 ms. The intensity of the 405 nm laser was 1.1 kW/cm^2. In figure 5.1 a schematic of the binding of quantum dot-streptavidin to lipid is represented.

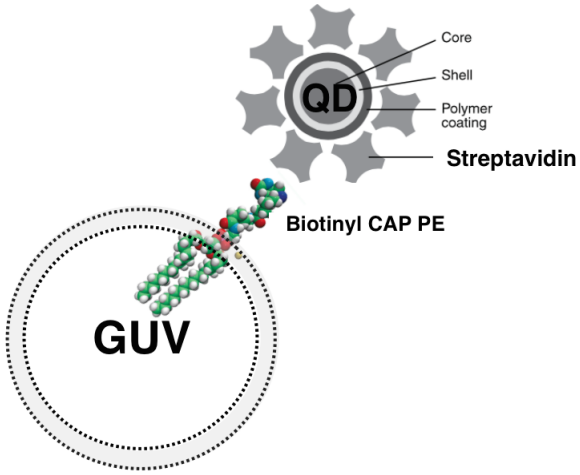

Figure 5.1: Binding of quantum dot-streptavidin to biotinylated CAP PE. Not to scale.

5.3 Results and Discussion

The diffusion of the quantum dots was observed imaging the top of the phase separated GUVs (figure 5.2). A typical image obtained is reported in figure 5.3. From the raw images, the positions of the quantum dots are found using a localization algorithm.

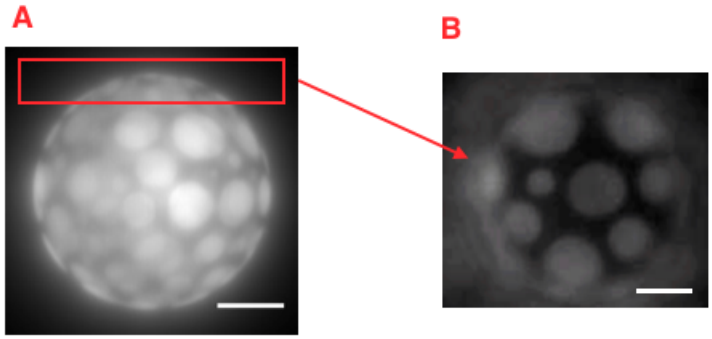

Figure 5.2: **A** 3D image of a phase separated GUV obtained from z-stack. The top part is pointed out with a red rectangle. **B** 2D image of the top the GUV on the left. The scale bar is 5 μm.

Firstly the signal and the slowly changing or static background parts are separated by low-spatial-frequency filtering. The background-subtracted images are then filtered by cross-correlation with the Point Spread Function (PSF) of the laser, that is approximated with a Gaussian. By setting a threshold, only the interesting signals are kept and everything else is considered noise. In this way it is possible to detect the signals from the fluorophore molecules. Finally each single-molecule peak is fitted to the PSF, and information about position, signal intensity, spatial width of the signal, and background signal are retrieved. The efficiency of the whole image processing depends directly on the setting of 36 parameters that are involed in the analysis. The different steps of the whole process are shown in figure 5.4.

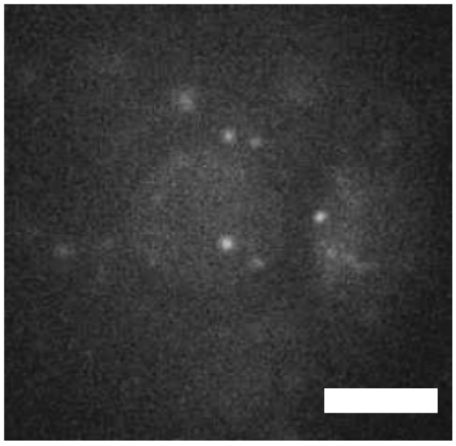

Figure 5.3: Example of a typical image of the top of a GUV with quantum dots analysed. the scale bar is 5 μm. Even if the image is obtained by using only the 405 laser for the quantum dots, also the L_d domains are quite visible; this is because the 405 nm laser belongs to the excitation band of Rhodamine.

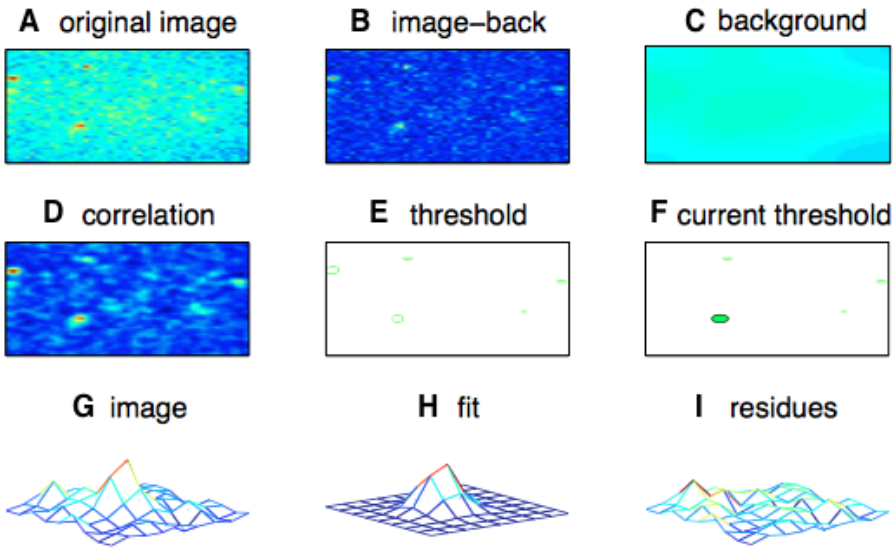

Figure 5.4: Illustration of the typical steps during image processing and peak localization. **A** input image, **B** background subtracted image, **C** background, **D** correlation map, **E** areas above the noise threshold, **F** current peak highlighted, **G** intensity distribution of the current peak, **H** Gaussian fit to the current peak, **I** residuals of the fit [45].

The obtained positions are further filtered by setting some threshold parameters for the intensity of the laser, the width of the PSF of the quantum dots and the accuracy in the localization of the molecules (error in the coordinates of the quantum dot's position).
These remaining *clean* positions are the starting point for tracking. A probabilistic algorithm is used to connect the positions of molecules in two subsequent frames of a movie. Two key ingredients that optimize the tracking are:

- a good signal to noise ratio
- a low (approximately 20) number of single molecules (quantum dots) for frame. The quantity of quantum dots in the preparation of the sample is chosen to give this result because a large number of quantum dots makes the tracking calculation more difficult and less efficient.

Starting from the trajectories $r(t) = [x(t), y(t)]$ (figure 5.5 A), the mean square displacements (MSD) were calculated:

$$MSD = \rho(t) =< (r(t) - r(0))^2 >$$

We have analysed the MSD in terms of anomalous diffusion. For every trajectory with N MSD, we use did a linear interpolation with the first $\sqrt{N}$ steps (figure 5.5 B). The good data are only in the first part of the trajectory because the error on the MSD grows with time. The MSD were fitted with:

$$\rho(t) = 4Dt^{\alpha}$$

where for:

- $\alpha > 1$ there is super diffusion
- $\alpha = 1$ there is normal diffusion
- $\alpha < 1$ there is subdiffusion

We analysed 500 tracks of quantum dots in 10 different GUVs and calculated the value of α for each track. In figure 5.5 C we show the probability density function (PDF) of α. The PDF shows that the most probable types of motion is subdiffusion. The only explanation of the presence of subdiffusive motion in our system is confinement. The compartmentalisation is in particular clear if we image the sample using two lasers that excite the dye (Rhodamine) and the quantum dots separately, like in figure 5.5 D. We observed that there is no preference for quantum dots for a particular phase. This is unexpected since we bounded the quantum dots to a particular lipid with a particular preference (DOPE, L_d). However the light might have converted some of the DOPE. For proteins, it entirely depends on the protein what it's preference is, or even if there is a preference.
Using proteins instead of quantum dots would be an interesting study to do in the future, since it mimics better the real biological situation better.

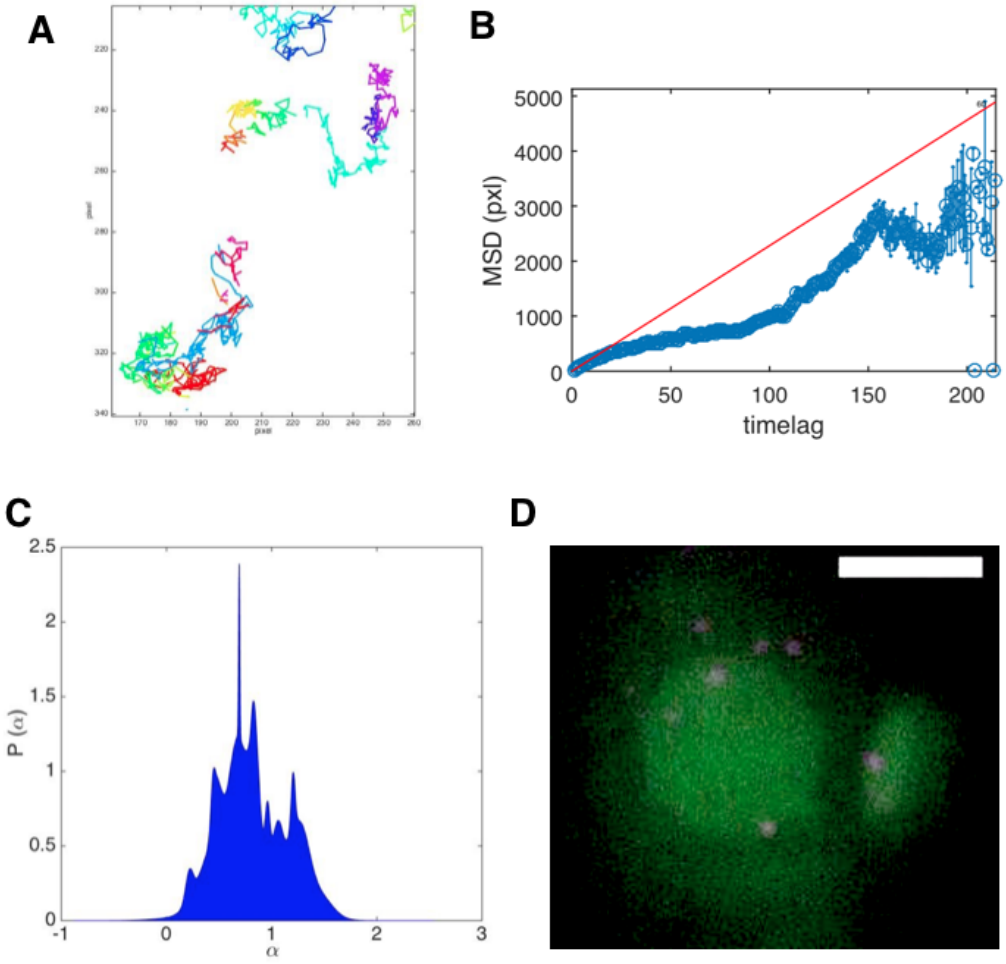

Figure 5.5: **A** Example of some trajectories. **B** MSD plot of a trace. One pixel is 69.3 nm **C** Probability density function of α **D** Image of the top of a GUV that has a big domain in the center (labeled in green) and quantum dots (in pink). The scale bar is 5 μm.

5.4 Conclusion

We observed confinement of quantum dots in the two different phases. The analysis presented here is only a *starting point* to further studies that are encouraged by the clear visualisation of the confinement in the different phases obtained during the experiments and a signature of subdiffusive motion. A study on these data related to confinement will be carried out in our lab using the method described by Quian et al. [71].

Conclusions

Lipid bilayer membranes undergo complex physical behaviour called phase separation, the transition from one single uniform liquid state to two coexisting liquid phases: the liquid ordered and the liquid disordered phases [12, 13, 18]. The role of this phase-partitioning in living cells was subject of a long debate. At present, controversial opinions are proposed about the raft hypothesis, the ability of some liquid domains with high chain order to mediate protein-protein interactions, and therefore cell signalling [55].
Giant Unilamellar vesicles (GUVs) are artificial versatile models for studying phase separation. The state of the art technique to obtain phase separation in vesicles uses temperature as order parameter.
In this work, a new cutting edge method is systematically adopted. We obtained phase separation by applying light. To this aim, we vary the composition of the lipid membrane by means of the mechanism of photo-oxidation and we keep the temperature constant.
The control gained with this technique allows us to observe all of the process of phase separation. Furthermore this method is experimentally more convenient than previously used methods involving temperature change, since it makes possible to induce the phase separation in one vesicle at a time instead of all the sample simultaneously.
We pointed out that the dynamics of phase separation by light depends on several parameters including the lipid composition, the quantity of dye, the intensity of light and the difference in osmotic pressure. We found and quantified a dependence of the time needed to obtain the phase separation on light intensity.
We followed the dynamics of the GUV during the whole process of phase separation, from when it is uniform to its phase separated state. We observed that when the composition changes and reaches the critical value, where the transition happens, the vesicle shows large shape variations. We studied these fluctuations as signature of a critical process. Firstly, we investigated the driving force that underlie these fluctuations. These fluctuations are induced by the area increase of the single oxidized lipid molecules that cause an increase of the total surface area of the vesicles. We quantified the increase of the area during the illumination time.
We calculated the spectra of the fluctuations in the real and in the frequency domain. From fitting the Fourier transform to a model previously developed in our lab [12] we obtained the behaviour of the surface tension and the bending modulus during the process of phase separation. While the bending modulus shows no characteristic variation during the process, the surface tension displays a fast decrease. The critical behaviour of the surface tension was studied and quantified.
Finally from universality arguments and experimental tests we concluded that the process is a non-equilibrium process.

In the second part of the of the work we used the technique of phase separation by light to study a biological problem, the receptor compartmentalisation in spines. As previous studies hypothesised [8], we think that in the head of the spines there are some confinement regions for receptors. This is one of the possible explanations of receptor compartementalisation in the spine head. We built an artificial model to study the problem in a simplified environment using GUVs to model the head of the spines, quantum dots to model receptors and the phase separated domains to mimic the confinement regions.
We used single molecule fluorescence microscopy techniques to follow the trajectories of the quantum dots up to 3 ms of time resolution and an accuracy in the localization of about 20 nm. In the experiments we visualised and recorded the confinement of the quantum dots in the different phases. We also performed a first quantification, analysing the motion of the quantum dots in terms of anomalous diffusion. We found the presence of the subdiffusive motion signifying confinement. Future experiments could directly show the presence of the confinement and the size of the confinement regions.

Appendix: supplementary information

A1 Domain Imaging

One advantage of the technique of phase separation induced by light is that it allows to see the entire sequence of the transisition with selectable velocity. In this way it is possible to image the process of domain formation. As said, we employ DOPE-Rhod as fluorophore to image the GUVs. Since the DOPE goes in the liquid disordered phase, it is the liquid disordered phase that is labelled by the dye. Therefore in all the gray-scale images of phase separated GUVs, like the one in figure 4.7, the liquid ordered domains are dark and the liquid disordered domains are bright.
The domain formation starts with the nucleation of nanodomains. These domains diffuse and fuse. In order to obtain straightforward imaging of the different phases, we carried out an experiment in which we employed two different dyes; one to label the liquid ordered phase, Alexa 647 Cholera Toxin Subunit B attached to GM1 [1] and one for the liquid disorderd phase, DOPE-Rhod (Recipe 3 Appendix A7.3) .
In figure 5.6 we can see that at time t=0 (fig. 5.6 A) there is no phase separation and the two colors that label the dyes overlap. In figure B and C we can see the formation of the microdomains that aggregate to become larger domains visible in figure D (L_o domains in red and L_d domains in green). We have adjusted the contrast and brightness of the images D and E to make the domains more visible and eliminate uninteresting signals. Different types of dye listed in table 5.1 were

L_o	L_d
Alexa 647-GM1	Rhodamine-DOPE
	Perylene
	DiD
	DiI
	Fm-464

Table 5.1: Classification of the dyes employed during experiments based on which phase they label.

tested. As reported in the study of Baumgart [63] there is only a small number of dyes available to label the liquid ordered phase.

[1] The Alexa Cholera Toxin is a dye that has a molecule of Cholera toxin attached via a covalent bond. Cholera toxin binds to ganglioside GM1, making it a powerful tool for labelling the liquid ordered phase.

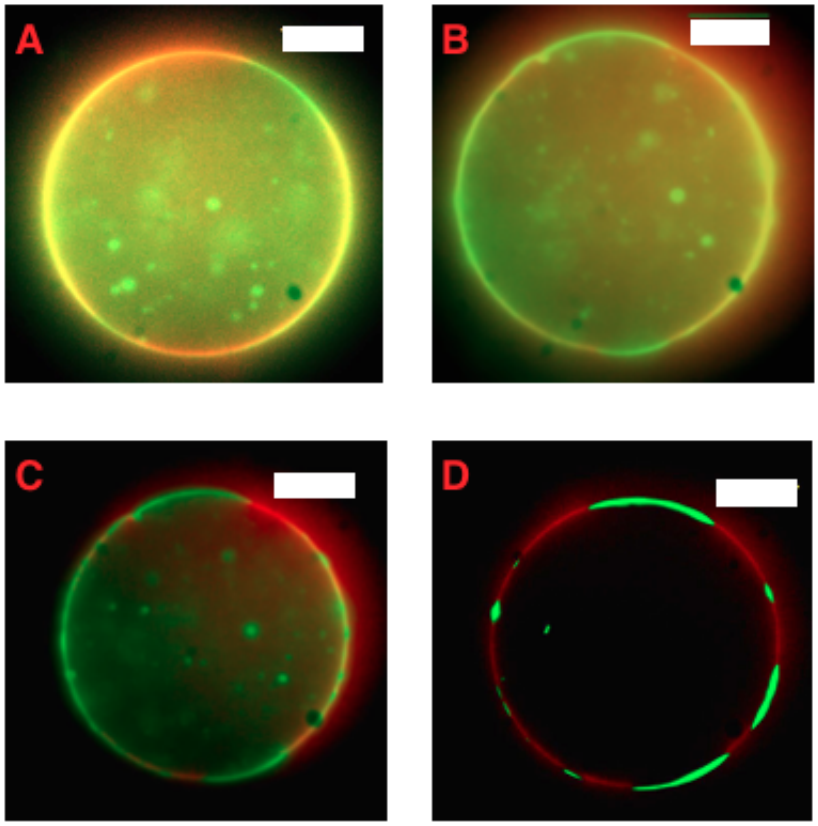

Figure 5.6: **Sequence of phase separation of one GUV labelled with two dyes.** The image A was taken at t=0. Between every image there are 20 seconds. The scale bar is 10 μm. The L_o domains are in red and the L_d domains in green.

A2 Domain fluctuations

We reported that GUVs near the critical point exhibit large shape fluctuations. During our experiments we observed not only fluctuations of the whole GUV, but also of the edge of the domains.

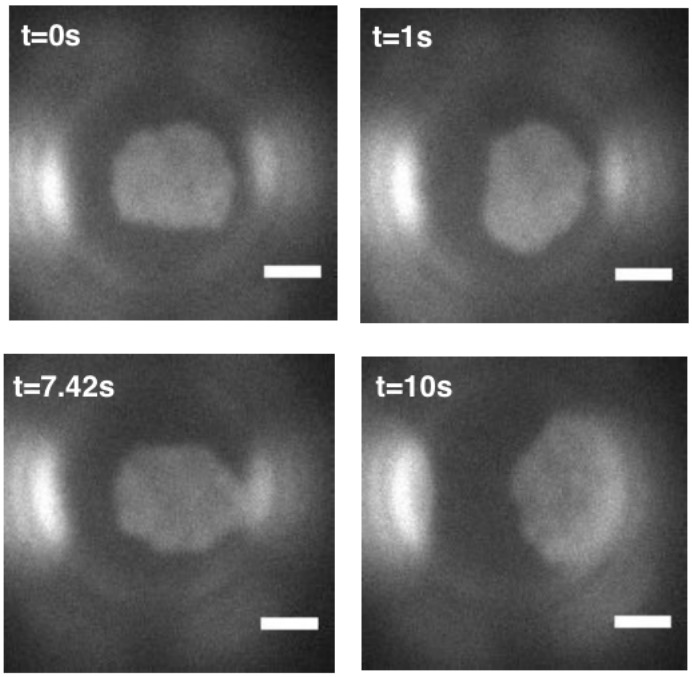

Figure 5.7: GUV imaged from the top at different times. The scalebar is 5 μm.

As reported by Veatch et al. [50] for temperature driven phase separation these fluctuations were followed and analysed as evidence of the criticality of the system. Like in the *temperature-experiment*, we noticed that these fluctuations are present only near the critical point. When GUVs are far from phase transition, these domain fluctuations disappear and the domains have a stable circular shape. Figure 5.7 shows a view of a GUV from the top with a big domain in the center. The fluctuations of this domain from a circular shape are optically visible.
In this sequence it is also possible to observe another interesting phenomenon mentioned: the fusion of the domains. The domain in the center coalesce with the one on its right (fig. 5.7 t=7.42 s) to fuse into one bigger domain (fig. 5.7 t=10 s).

A3 Tube formation

Another aspect we observed in the experiments is that when we employ a high difference of osmolality between the inside and the outside ($\approx$ 30 mOsmol/Kg) and we apply light, we observe the presence of phase separation with the formation of some inner tubes. In some cases there is no phase separation, but only formation these tubes. In figure 5.8 A we reported the formation of these tubules. For this reason we mantained similar osmolarities inside and outside the GUVs.
This phenomenon is present also when the phase separation is induced by temperature [70], as it can be observed directly in figure 5.8 B.

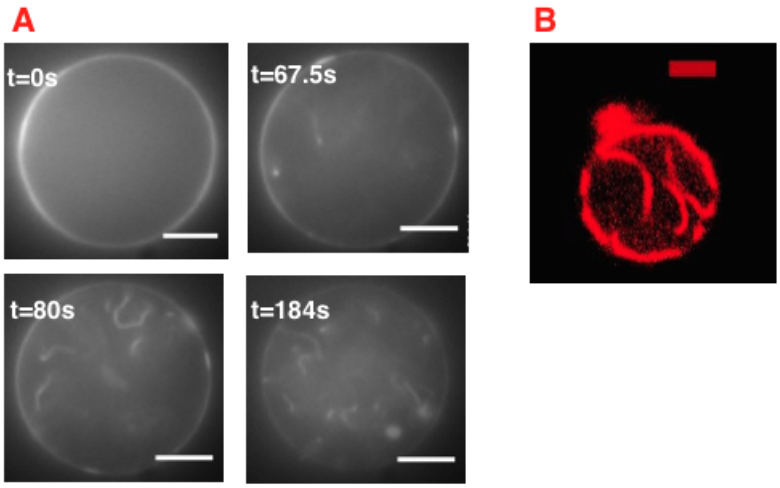

Figure 5.8: **A** GUV stressed with light to obtain the phase separation that displays the formation of tubes. **B** Phase separated GUV with the temperature that shows the presence of tubules. The image is obtained with a confocal microscope. The scalbar is 5 μm.

A4 Budding

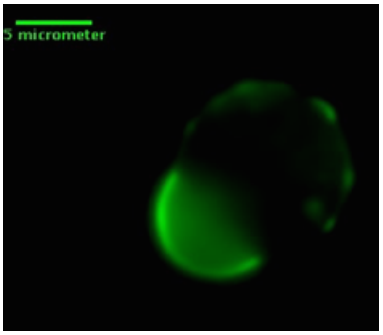

Figure 5.9: GUV with a big bud. The scale bar is 5 μm

With a positive osmolality difference between the inside and the outside the GUV which can range from few to tens mOsmol/Kg we observed *budding* of the vesicles (figure 5.9): some domains *bud out* and the membrane deform around them locally. This phenomenon is also reported in other previous studies [12–14, 62] on temperature-driven phase separation. These domains posses long term stability unlike flat domains that have the same curvature as the vesicle and like to fuse together.

A6 On light intensity and dye

There are several parameters that influence the dynamics of this process and should be adjusted to obtain a sequence like the one described above. In particular the intensity of light, the quantity of fluorophore and the osmolality difference between inside and outside the GUVs. We have observed how these variables influence the process.
The intensity of light dictates the velocity of the process (figure 5.10), and therefore the time needed to achieve phase separation. Since the number of photons per second in a laser beam is described with

$$n = \frac{P}{h\nu}$$

where P is the laser power and ν is the frequency of the light, a high intensity means a high probability to oxidize the lipid molecules and therefore shorter time required to reach the critical coexistence region. The graph in figure 5.10 shows the dependence of the time needed to start the phase separation on the intensity of the *oxidizing* laser.

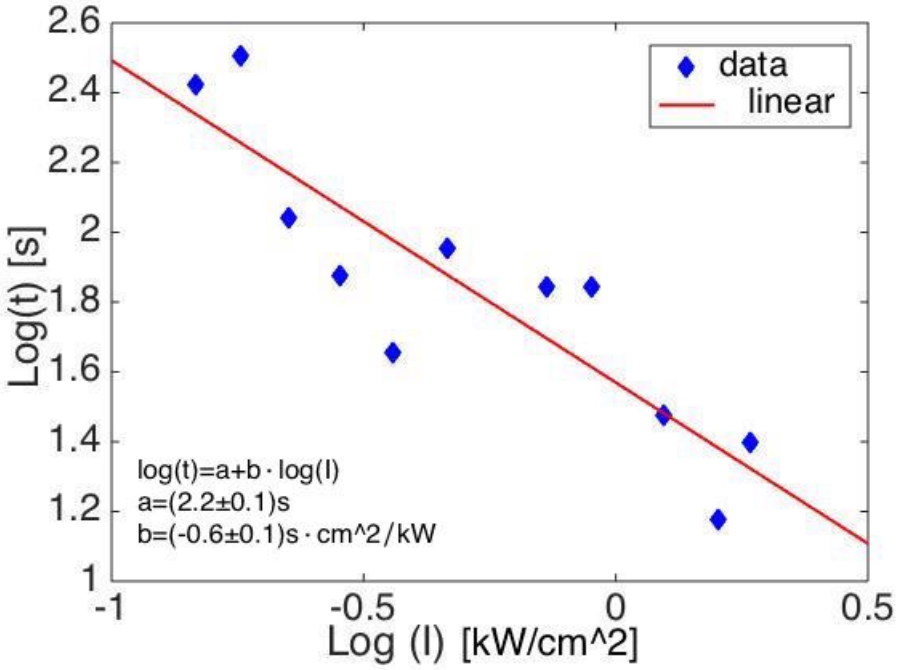

Figure 5.10: Dependence of the time to obtain phase separation on intensity of the 561 nm laser.

The quantity of dye employed is of critical importance to obtain phase separation. Since the number of fluorophore molecules that transfer their energy to the oxygen are proportional to the probability to convert the lipids, the quantity of dye chosen should be enough to reach a critical composition. If not, the dye bleaches and phase separation does not occur.

We define the probability to oxidate the lipid molecules of a vesicle as:

$$p = \frac{dn}{dt}$$

where n is the number of molecules oxidated. The probability p is proportional to the number of molecules oxidated and the constant of probability is the result of different contributes to the process:

$$\frac{dn}{dt} = Cn \qquad C = n_{lipids} \cdot n_{dye} \cdot \nu \cdot I$$

where

- n_{lipids} is the number of lipid molecules that go in the liquid disorder phase and than can be oxidated
- n_{dye} is the number of molecules of the dye
- ν is the lifetime of the triplet state of the dye
- I is the intensity of light

Integrating on both sides leads to:

$$n = n_0 \cdot \exp\left(\frac{t}{\tau}\right) \qquad \tau = \frac{1}{C}$$

with n_0 is the number of molecules oxidated at the time $t = 0\ s$.

A7 Chemical protocols

A7.1 Glass cleaning

The ITO glasses and the coverslips were cleaned with:

- 15 minutes of sonification in 2% Helmanex solution in milliQ and three washes in milliQ
- 15 minutes of sonification in Ethanol and three washes in milliQ
- 15 minutes of sonification in milliQ

A7.2 Immobilisation

To immobilise the GUVs on the coverslips we:

- added 1 ml of Bovine Serum Albumin (BSA) on the coverslips mounted in the sample holders
- left them with the BSA for 15 minutes
- washed them with PBS three times

A7.3 Recipes

GUVs

GUVs were produced via electrosweeling. 100 μl of mixture with the following recipe:

- 2 μl Chol 10g/l
- 3.5μl POPC 10g/l
- 4 μl SM 10g/l
- 5 μl DOPE-Rhodamine 1g/l
- 85.5 μl $CHCl_3$

GUVs with CAP PE for single molecule experiments

GUVs were produced via electrosweeling. 100 μl of mixture with the following recipe:

- 2 μl Chol 10g/l
- 3.5μl POPC 10g/l
- 4 μl SM 10g/l
- 5 μl DOPE-Rhodamine 1g/l
- 1 μl Biotynil CAP PE 10g/l
- 84.5 μl $CHCl_3$

GUVs with Alexa Cholera Toxin and GM1

GUVs were produced via electrosweeling. 100 μl of mixture with the following recipe:

- 2 μl Chol 10 g/l
- 5 μl GM1 1 g/l
- 3.5μl POPC 10 g/l
- 4 μl SM 10 g/l
- 5 μl DOPE-Rhodamine 1g/l
- 80.5 μl $CHCl_3$

Before the observation on the microscope, 1 μl of Alexa cholera toxin from the stock solution was added to 200 μl of washed GUVs.

A8 Polarization of light

Polarization is a fundamental property of light [72]. Light is considered to be linearly polarized when the orientation of its electric field vector does not change during propagation. The interaction of polarized light with a fluorophore can be best described by considering the concept of an electric dipole. Fluorophores tend to have a dipole moment, and the excitation dipole moment of a fluorophore can be different from its emission dipole moment. When the electric field of the excitation light is parallel to a fluorophore's absorption dipole moment the fluorophore has the greatest chance of absorbing a photon, which leads to its preferential excitation among the population of illuminated fluorophores. On the other hand, when the absorption dipole moment is perpendicular to the electric field of excitation then the fluorophore cannot be excited [73] (figure 5.11).

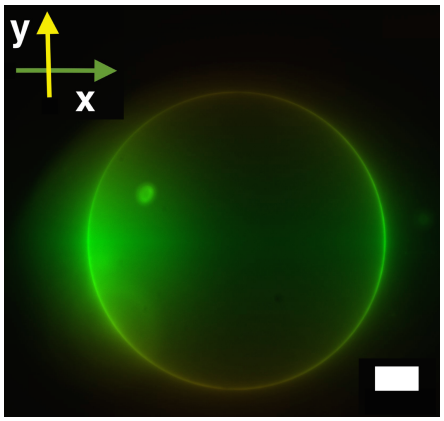

Figure 5.11: GUV labelled with Perylene (yellow) and Rhodamine. The scale bar is $5\mu m$.

Bibliography

[1] P. Hotulainen, C. Hoogenraad "Actin in dendritic spines connecting dynamics to function" *The Journal of Cell Biology, Vol.189, No. 4 619, 2010*

[2] H.Hering, M. Sheng "Dendritic Spines Structure, Dynamics and Regulation", *Nature Reviews Vol. 2 December 2001*

[3] M. Segal "Dendritic Spines and long-term plasticity", *Nature Reviews, Vol. 6 April 2005*

[4] H. Kasai "Structural dynamics of dendritic spines in memory and cognition", *Trends in Neurosciences Vol. 33 No.3, pag:121-129*

[5] W. Pomp, T. Schmidt "Morphology Induced Receptor Trapping in Artificial Dendritic Spines", *Biophysical Journal, vol 108, issue 2, pag: 342a-343a, 2015*

[6] M. Angelova, D. Dimitrov, (1986). "Liposome electroformation". *Faraday Discuss. Chem. Soc., pag: 303 - 311*

[7] J. T. Trachtenberg, B. E. Chen et al. "Long-term in vivo imaging of experience-dependent synaptic plasticity in adult cortex"*Nature, vol. 420 19/26 December 2002, pag. 788-794*

[8] M. Adrian, R. Kusters et al. "Barriers in the brain resolving dendritic spine morphology and compartmentalization" *Frontiers in Neuroanatomy, December 2014, vol.8 Article 142 pag. 1-12*

[9] S. H. Shim, C. Xia et al. "Super-resolution fluorescence imaging of organelles in live cells with photoswitchable membrane probes" *Proc Nat Acad Sci USA 109, 13978-13983, 2012*

[10] R. Kusters, L.C. Hoogenraad and al. "Shape induced asymmetric diffusion in dendritic spines allows efficient synaptic AMPA receptor trapping" *Biophysical Journal 105, 2743-2750, 2013*

[11] F. Vacca, S. Amadio "P2X3 Receptor Localizes Into Lipid Rafts in Neuronal Cells" *Journal of Neuroscience Research 76 653:661 (2004)*

[12] S. Semrau "Membrane heterogenity" *Casimir PhD series, Delft-Leiden 2009*

[13] T. Baumgart, S. T. Hess W. W. Webb "Imaging coexisting fluid domains in biomembrane models coupling curvature and line tension" *Nature 425, 821 -824 (2003)*

[14] S. L. Veatch, S.L. Keller "Separation of Liquid Phases in Giant Vesicles of Ternary Mixtures of Phospholipids and Cholesterol" *Biophysical Journal Vol. 85 November 3074 -3083 (2003)*

[15] S. Semrau, T. Idema et al. "Membrane mediated Interactions Measured Using membrane Domains" *Biophysical Journla vol. 96, June 2009 4906-4915*

[16] S. Veatch, S. L. Keller "Organization in lipid membranes containing cholesterol" *Phys. Rev. Letter 89 268101, 2002*

[17] S. Veatch, I. V. Polozov et al. "Liquid domains in vesicles investigated by NMR and fluorescence microscopy " *Biophysical Journal 86 2910-2922 (2005)*

[18] S. Veatch, S. L. keller "Miscibility phase diagrames of giant vesicles containing sphingomyelin" *Phys. Rev. Letters 94 148101, 2005*

[19] S. Veatch, K. Gawrisch et al. "Closed-loop miscibility gap and quantitative tielines in ternary membranes containing diphytanoyl PC" *Biophysical Journal 90 4428-4436, 2006*

[20] K. Bacia, P. Schwille et al. "Sterol structure determines the separation of phases and the curvature of liquid ordered phase in lipid membrane" *Nature 425 821-824, 2003*

[21] T. Baumgart, S. das et al. "Membrane elasticity in giant vesicles with fluid phase coexistence" *Biophysical Journal 89 1067-1080*

[22] M. Edidin "The state of lipid rafts from model membranes to cells" *Annu. Rev. Biophysics. Biomol. Structure 32 257-283*

[23] S. Munro "Lipid rafts, elusive or illusive" *Cell. 115 377-388*

[24] C. Esposito et al. "Flicker Spectroscopy of Thermal Lipid Bilayer Domain Boundary Fluctuations" *Biophysical Journal, vol.93 pag.3169-3181, 2007*

[25] A. G. Ayuyan, F. S. Cohen "Lipid Peroxides promote Large Raft Effects of the Excitation of Probes in Fluorescence Microscopy and Electrochemical Reactions during Vesicles Fromation" *Biophysical Journal vol.91 September 2006 2171-2183*

[26] M. DeRosa, R. J. Crutchley "Photosensitized singlet oxygen and its application" *Coordination Chemistry Revies 233-234 (2002) 351-371*

[27] C. K. Haluska, M.S. Baptista et al. "Photo-activated phase separation in giant vesicles made from different lipid mixtures" *Biochimica et Biophysica Acta 1818 (2012) 666-672*

[28] K. A. Riske, T.P. Sudbrack et al. "Giant Vesicles under Oxidative Stress Induced by a Membrane-Anchored Photosensitizer" *Biophysical Journal vol. 97 September 2009, pag. 1362-1370*

[29] J. Zhao, J. Wu, H. Shao et al. "Phase studies of model biomembranes macroscopic coexistence of $L_\alpha + L_\beta$, with light-induced coexistence of $L_\alpha + L_\beta$ Phases"*Biochim Biophys Acta 2077 November; 1768(11) 2777-2786*

[30] J. Heuvingh, S. Bonneau "Asymmetric Oxidation of Giant Vesicles Triggers Curvature-Associated Shape transition and Permeabilization" *Biophysical Journal vol. 97 December 2009 2904-2912*

[31] K. A. Runas, N. Malmstadt "Low levels of lipid oxidation radically increase the passive permeabilty of lipid bilayers" *Soft Matter, 2015, 11, pag. 499-505*

[32] *https //www.khanacademy.org/science/health-and-medicine 2015*

[33] B. Alberts et al. "Molecular Biology of the Cell" 6th edition *Garland Science, 2014*

[34] *Nikon Microscopy U https://www.microscopyu.com*

[35] J. Lichtman, J.A. Coachello "Fluorescence microscopy" *Nature methods vol.2 no.12 December 2005*

[36] B. C. Chen, W. R. Legant "Lattice light-sheet microscopy Imaging molecules to embryos at high spatiotemporal resolution" *Science, 24 October 2014, vol. 346 issue 6208*

[37] R. P. Feynman "Plenty of room at the bottom" *American Physical Society, Caltech on December 29, 1959*

[38] N. G. Walter, C. Huang et al., "Do-it-yourself guide how to use the modern single-molecule toolkit" *Nature Methods, vol. 5 no. 6, June 2008 pag. 475-489*

[39] C . R. de Oliveira, T. Werlang "Ergodic hypothesis in classical statistical mechanicst" *Revista Brasileira de Ensino de F ÌĄÄśsica, v. 29, n. 2, p. 189-201, (2007)*

[40] T. Schmidt, G. J. Schütz "Imaging of single molecule diffusion" Proc. Natl. Acad. Sci. USA vol 93 pag. 2926-2929

[41] Qian, H., Sheetz, M. P. "Single Particle Tracking. Analysis of Diffusion and Flow in Two-Dimensional System" *Biophysic Journal, 60, 910-921 (1991)*

[42] P. R. Selvin "Single molecule techniques a laboratory manual" *Cold Spring Harbor Laboratory Press , New York, 2008*

[43] A. Yildiz et al. "Myosin V walks hand-over-hand single fluorophore imaging with 1.5 nm localization " *Science 300, 2061-2065 (2003)*

[44] R. Thompson, D.R. Larson et al. "Precise Nanometer Localization Analysis for Individual Fluorescente Probes" *Biophysical Journal, 82, 2775-2783 2002*

[45] A. Pezzarossa "Imaging plasma membrane domains in signal-transduction pathways" *Casimir PhD series, Delft-Leiden 2012*

[46] A. Einstein " On the theory of the Brownian movement " *Annalen der Physik (4), 19, 1906 pp. 371-381*

[47] D. Gillespie "The mathematics of Brownian motion and Johnson noise" *American Journal of Physics 64 (3) 1996*

[48] K. Huang "Statistical Mechanics" *John Wiley & Sons 1963*

[49] V.L. Ginzburg "What problems of physics and atrophysics seem now to be especially important and interesting?" *Physics Today, May 1990 pag. 9-11*

[50] A. R. Honerkamp-Smith, S. L. Veatch, S. L. Keller "An introduction to critical points for biophysicists; observations of compositional heterogeneity in lipid" *Biochimica et Biophysica Acta 1788 (2009) pag. 53 -63*

[51] A. R. Honerkamp Smith, S. Veatch et al. "Line tensions, Correlation Lengths, and Critical Exponents in Lipid Membranes Near Critical Point" *Biophysical Journal, vol.95 pag. 236-246, 2008*

[52] J. M. Yeomans "Statisical Mechanics of Phase Transitions" *Clarendon Press, Oxford, 1992*

[53] C. A. Croxton "Statistical Mechanics of the liquid surface" *John Wiley and Sons*

[54] R. Dimova, S. Aranda, N. Bezlyepkina "A practical guide to giant vesicles. Probing the membrane nanoregime via optical microscopy" *Journal of Physics condensed matter vol. 18 n. 28*

[55] E. Sevcsik, M. Brameshuber "GPI-anchored proteins do not reside in ordered domains in the live cell plasma membrane" *Nature Communications, Volume 6, id. 6969 (2015).*

[56] P. B. Canham. The minimum energy of bending as a possible ex- planation of the biconcave shape of the human red blood cell. *Journal of Theoretical Biology, 26 61 -81, 1970*

[57] W. Helfrich. Elastic properties of lipid bilayers Theory and possible experiments. *Z. Naturforsch. C, 28 693 -703, 1973.*

[58] K. A. Runas, N. Malmstadt "Low levels of lipid oxydation radically increase the passive permeability of lipid bilayers" *Nature methods, vol.2, n. 12, December 2005 pag. 910-919*

[59] De Gennes "The Physics of Liquid Crystals" *Clarendon Press, second edition, 1995*

[60] C. Dietrich, L. Bagatolli "Lipid rafts reconstituted in model membranes" *Biophysical Journal, 80(3), 1417 -1428*

[61] Samsonov, A. V., I. Mihalyov, et al. 'Characterization of cholesterol-sphingomyelin domains and their dynamics in bilayer membranes" *Biophysics Journal 81 1486 -1500, 2001*

[62] S. Semrau, T. Schmidt et al. "Membrane heterogenity-From lipids domain to curvature effect" *Soft Matter, 5 (17), 3174-3186, (2009)*

[63] T. Baumgart, G. Hunt et al. "Fluorescence probe partitioning between Lo/Ld phases in lipid membranes" *Biochim Biophys Acta 2007 Sep; 1768(9) 2182-2194*

[64] G. Weber "Photo-induced modifications of model membranes" *PhD Thesis, Université de Strasbourg, 2012*

[65] J. Wong-ekkabut. Z. Xu et al. "Effect of Lipid Peroxidation on the Properties of Lipid Bilayers A Molecular Dynamics Study" *Biophys J. 2007 Dec 15; 93(12) 4225 -4236*

[66] MATLAB and Statistics Toolbox, The MathWorks, Inc., Natick, Massachusetts, United States.

[67] S. Semrau "Accurate determination of elastic parameters for multi-component membranes" *Physics Review Letters 100 088101 (2008)*

[68] I. Prigogine "From being to becoming time and complexity in the physical sciences" *W.H. Freeman and Company*

[69] J. Pécréaux, H.-G. Dobereiner "Refined contour analysis of giant unilamellat vesicles" *European Physisics Journal E. 13 277-290, 2004*

[70] R. Lipowski "Spontaneous tubulation of membranes and vesicles reveals membrane tension generated by spontaneous curvature" *Faraday Discuss. 2013;161 305-31; discussion 419-59*

[71] H. Quian, M. Sheetz "Single Particle Tracking analysis of diffusion and flow in two-dimensional systems" *Biophysics Journal Vol 80, pag. 910-921, October 1991*

[72] Erdogan, T "Understanding Polarization" *Semrock White Paper Series*

[73] Erdogan, T "Fluorescence polarization in Life Technologies" *Semrock White Paper Series*